

1995

Modeling x-ray scattering process and applications of the scattering model

Taher Lutfi Al-Jundi
Iowa State University

Follow this and additional works at: <https://lib.dr.iastate.edu/rtd>

 Part of the [Atomic, Molecular and Optical Physics Commons](#), and the [Nuclear Engineering Commons](#)

Recommended Citation

Al-Jundi, Taher Lutfi, "Modeling x-ray scattering process and applications of the scattering model " (1995). *Retrospective Theses and Dissertations*. 10877.
<https://lib.dr.iastate.edu/rtd/10877>

This Dissertation is brought to you for free and open access by the Iowa State University Capstones, Theses and Dissertations at Iowa State University Digital Repository. It has been accepted for inclusion in Retrospective Theses and Dissertations by an authorized administrator of Iowa State University Digital Repository. For more information, please contact digirep@iastate.edu.

INFORMATION TO USERS

This manuscript has been reproduced from the microfilm master. UMI films the text directly from the original or copy submitted. Thus, some thesis and dissertation copies are in typewriter face, while others may be from any type of computer printer.

The quality of this reproduction is dependent upon the quality of the copy submitted. Broken or indistinct print, colored or poor quality illustrations and photographs, print bleedthrough, substandard margins, and improper alignment can adversely affect reproduction.

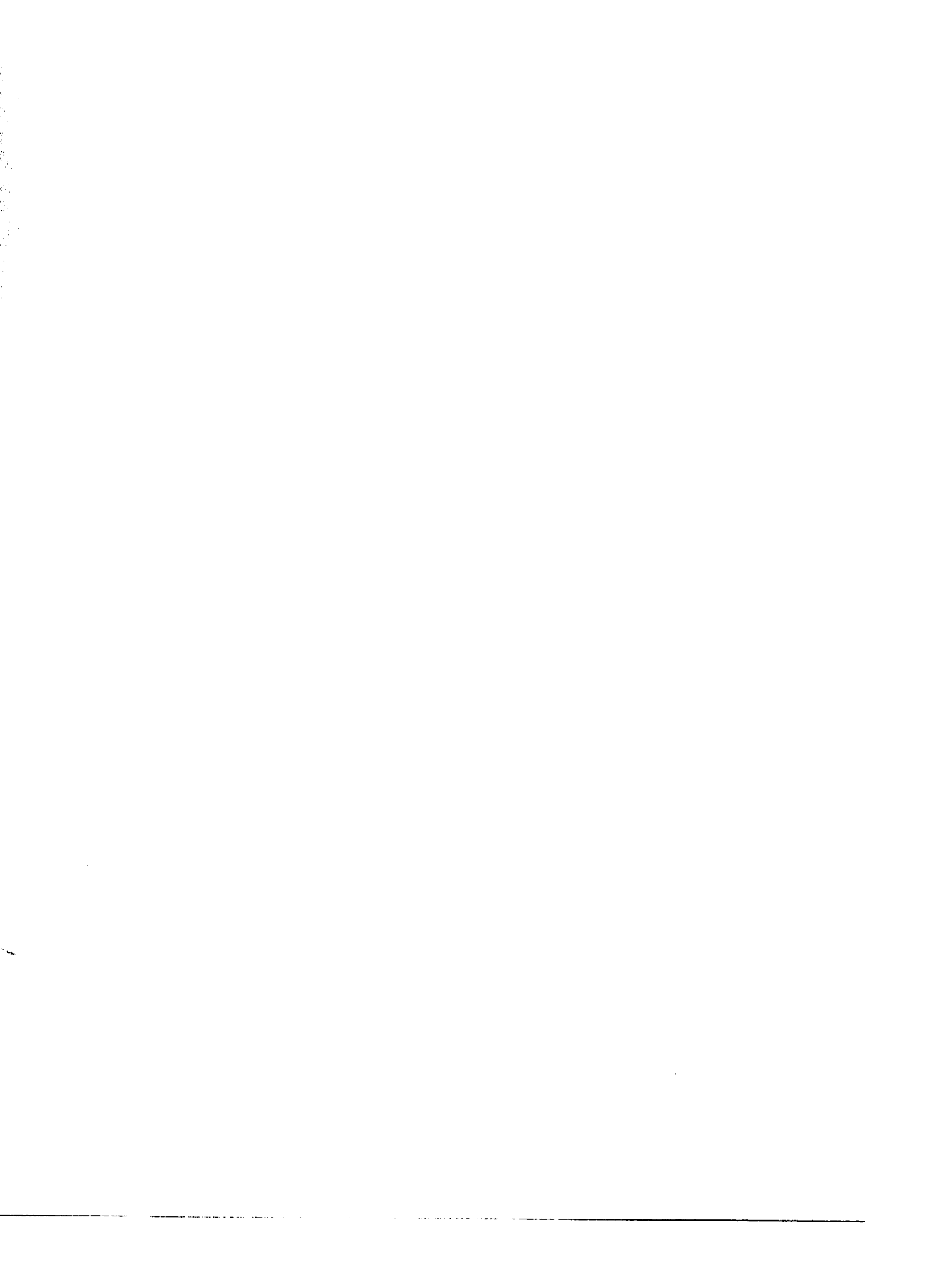
In the unlikely event that the author did not send UMI a complete manuscript and there are missing pages, these will be noted. Also, if unauthorized copyright material had to be removed, a note will indicate the deletion.

Oversize materials (e.g., maps, drawings, charts) are reproduced by sectioning the original, beginning at the upper left-hand corner and continuing from left to right in equal sections with small overlaps. Each original is also photographed in one exposure and is included in reduced form at the back of the book.

Photographs included in the original manuscript have been reproduced xerographically in this copy. Higher quality 6" x 9" black and white photographic prints are available for any photographs or illustrations appearing in this copy for an additional charge. Contact UMI directly to order.

UMI

**A Bell & Howell Information Company
300 North Zeeb Road, Ann Arbor, MI 48106-1346 USA
313/761-4700 800/521-0600**



**Modeling x-ray scattering process and
applications of the scattering model**

by

Taher Lutfi Al-Jundi

A Dissertation Submitted to the
Graduate Faculty in Partial Fulfillment of the
Requirements for the Degree of
DOCTOR OF PHILOSOPHY

Department: Mechanical Engineering
Major: Nuclear Engineering

Approved:

Signature was redacted for privacy.

Signature was redacted for privacy.

In Charge of Major Work

Signature was redacted for privacy.

For the Major Department

Signature was redacted for privacy.

For the Graduate College

Members of the Committee:

Signature was redacted for privacy.

Iowa State University
Ames, Iowa
1995

Copyright © Taher Lutfi Al-Jundi, 1995. All rights reserved.

UMI Number: 9531713

Copyright 1995 by
Al-Jundi, Taher Lutfi
All rights reserved.

UMI Microform 9531713
Copyright 1995, by UMI Company. All rights reserved.

This microform edition is protected against unauthorized
copying under Title 17, United States Code.

UMI

300 North Zeeb Road
Ann Arbor, MI 48103

TABLE OF CONTENTS

ACKNOWLEDGMENTS	x
CHAPTER 1. INTRODUCTION AND BACKGROUND	1
Sources of X-ray	2
Nondestructive Evaluation	7
Radiography	9
X-ray Interactions with Matter	15
CHAPTER 2. X-RAY RADIOGRAPHY SIMULATION	18
Introduction	18
The X-ray Radiography Simulation Code "XRSIM"	21
Limitations of XRSIM	23
X-Ray Computer Tomography Simulation Code "CTSIM"	25
X-ray Scattering Simulation	26
CHAPTER 3. SCATTERING IN THE OBJECT	30
Introduction	30
Buildup Factors	35
Definition of Buildup Factors	35
Experimental Procedures	39
Calculating Exposure Buildup Factors	45

Results and Conclusions	55
Scattering Unsharpness	62
CHAPTER 4. FILM UNDERCUT	66
Introduction	66
Measurement of Film Unsharpness	67
Simulating the Scattering in the Film Plane	70
Results	75
CHAPTER 5. BACK SCATTERING SIMULATION	83
Introduction	83
User Interface	85
Algorithm	88
Results	89
Conclusion and Future Work	96
CHAPTER 6. CONCLUSIONS AND FUTURE WORK	99
BIBLIOGRAPHY	104

LIST OF TABLES

Table 3.1:	A balanced output of the parallel code	55
Table 4.1:	Intensities from the fluorescent for elements in a KODAK-AA film obtained using an electronic microscope at a tube voltage of 30 keV	71

LIST OF FIGURES

Figure 1.1:	The electromagnetic spectrum	2
Figure 1.2:	A schematic diagram of a typical x-ray generator tube	4
Figure 1.3:	A typical x-ray white spectrum	6
Figure 1.4:	The radiographic setup consists of a source, a specimen and a detector.	10
Figure 1.5:	Compton effect.	16
Figure 1.6:	The relative importance of the three major types of photon interactions. τ σ κ are the probabilities of a photoelectric event, Compton scattering, and pair production respectively .	17
Figure 2.1:	The simulated bremsstrahlung spectrum compared to a nor- malized spectrum obtained from an actual x-ray generator (HOMX-160)	22
Figure 2.2:	A radiographic image of a block of Al with 16 holes of different depths in it generated by XRSIM (left) compared to an image generated experimentally (right)	24
Figure 2.3:	Tomographic configuration	27

Figure 3.1:	Simulated primary and scattered fluxes emerging from a rectangular iron block at 100 kv (top) and 200 kv (bottom) as a function of the block thickness.	33
Figure 3.2:	Simulated primary and scattered fluxes emerging from a rectangular aluminum block with a tube voltage of 100 kv (top) and 160 kv (bottom) as a function of the block thickness. . .	34
Figure 3.3:	Configuration for which the detector response for a parallel beam of x-rays can be predicted using buildup factors	36
Figure 3.4:	Experimental setup for film calibration	41
Figure 3.5:	Calibration curve for the KODAK-AA x-ray film at a tube voltage of 100 kv	42
Figure 3.6:	Experimental setup for measuring “exposure buildup factors”	44
Figure 3.7:	C-Linda performance with increasing number of nodes	53
Figure 3.8:	Measured and simulated energy spectrums behind a 0.75 inch thick aluminum block at tube voltage of 100 kv	56
Figure 3.9:	Comparison between the outputs of the EGS4 and our code. The energy spectrums behind a 0.75 inch thick aluminum block at tube voltage of 100 kv	56
Figure 3.10:	Measured primary and scattered fluxes emerging from a rectangular steel block at 106 kv in which the steel block is placed in front of the detector (top) and in front of the source (bottom).	59
Figure 3.11:	Measured primary and scattered fluxes emerging from a rectangular aluminum block at 74 kv in which the block is placed in front of the detector (top) and in front of the source (bottom).	60

Figure 3.12: Measured and calculated buildup factors for aluminum	61
Figure 3.13: Experimentally obtained image (left) compared to the output of XRSIM after integrating the buildup factors to account for scattering (right).	61
Figure 3.14: Image Unsharpness	63
Figure 3.15: Calculated total and scattered fluxes emerging from an alu- minum step wedge with a step height of 4.5 cm and a base of 0.5 cm at a tube voltage of 100 kv	65
Figure 4.1: Construction of an x-ray film. a:hard gelatin to protect emul- sion. b:emulsion. c:substrate to attach emulsion to base, and d:polyester base.	67
Figure 4.2: Photons might suffer a Compton scattering at an angle such that they travel in the emulsion layer	68
Figure 4.3: Experimental values for film unsharpness obtained for KODAK- AA x-ray film at 100 kV tube voltage	69
Figure 4.4: Calculated undercut for two different types of x-ray films using the same tube voltage with different exposures	76
Figure 4.5: Calculated undercut for two different types of x-ray films using the same exposure and varying the tube voltage	76
Figure 4.6: Comparison between an image for the Al block generated ex- perimentally (left) and simulated with the undercut effect in- tegrated into XRSIM (right), using DEF-5 films	78

Figure 4.7:	Calculated undercut for the upper and lower halves of the spectrum compared to the total spectrum, DEF-5 films, kvp = 320 kv.	78
Figure 4.8:	Calculated undercut for the first and second quarters of the lower half of the spectrum, DEF-5 films, kvp = 320 kv. . . .	80
Figure 4.9:	Calculated undercut for equivalent energy values and the whole spectrum , DEF-5 films, kvp = 320 kv.	80
Figure 5.1:	Configuration of the simulated inspection setup.	87
Figure 5.2:	Penetration depth in steel at different tube voltages.	89
Figure 5.3:	The type of defect determines the shape of the resulting signal.	91
Figure 5.4:	Z-scan with the defect in the way of the back scattered beam.	92
Figure 5.5:	Sensitivity towards different flaw sizes when the flaw is in the way of the incident beam.	93
Figure 5.6:	Sensitivity towards different Ti inclusion sizes when the defect is in the way of the incident beam.	93
Figure 5.7:	Flaw is in the way of the back scattered beam.	94
Figure 5.8:	Optimizing the scattering angle to maximize the back scattered amplitude.	95
Figure 5.9:	Z-scan through multiple materials.	96
Figure 6.1:	A radiographic image of a block of Al with 16 holes of different depths, generated experimentally (left) and generated using XRSIM (right).	100

Figure 6.2: Generated using XRSIM with buildup factors (left) and using XRSIM with the film undercut simulation (right). 101

Figure 6.3: Generated experimentally (left) and generated using XRSIM with both the buildup factors and the film undercut simulation integrated into XRSIM. 101

ACKNOWLEDGMENTS

I wish to express my sincere gratitude to my friend and major professor Dr. Joseph N. Gray, not only for sharing his knowledge with me, but also for his friendship. His support, guidance, and encouragement were invaluable all through the performance of this research. I wish to extend my thanks to Dr. Terrence Jensen for sharing his invaluable expertise in x-ray scattering throughout the past two years. I also wish to thank the rest of my committee members Drs. Alfred Rohach, Lester Schmerr, Danniell Bullen and David Hsu.

My parents played a great role in my education. They always have supported me in all my decisions even when they disagreed with me. For that, and for the way they raised me, helped me, supported me, and encouraged me, I wish to give special thanks to them.

Last but not least, I can not find proper words to express my appreciation for Jennifer L. Aljundi (my wife) for her love, patience, and understanding.

CHAPTER 1. INTRODUCTION AND BACKGROUND

In 1895 Wilhelm Roentgen found that a highly penetrating radiation of unknown nature was produced when fast electrons interacted with matter. He called these unknown radiations “X-rays”, and found that this unknown radiation traveled in straight lines, even through electric and magnetic fields, and passed through opaque materials. It was also found that the faster the original electrons, the more penetrating the resulting x-rays, and the greater the number of electrons, the greater the intensity of the x-ray beam. Later it was found that X-rays are a form of electromagnetic radiations and diffraction experiments were designed to measure their wavelengths. As shown in Figure 1.1, the x-ray wavelength lies in the upper end of the electromagnetic spectrum with an energy range roughly between few electron volts up to 15 MeV [1]. These boundaries are somewhat arbitrary, some scientists distinguish between x-rays and γ - rays according to the wavelength as shown in Figure 1.1, others call the photons that originate in the nucleus as γ -rays and those originating outside the nucleus as x-rays.

Almost immediately after the discovery of x-rays, people realized that this radiation can be used to penetrate the human body and solid materials and since then radiology and radiography have become important parts of medicine and nondestructive evaluation respectively. It was realized that because x-rays travel easily through

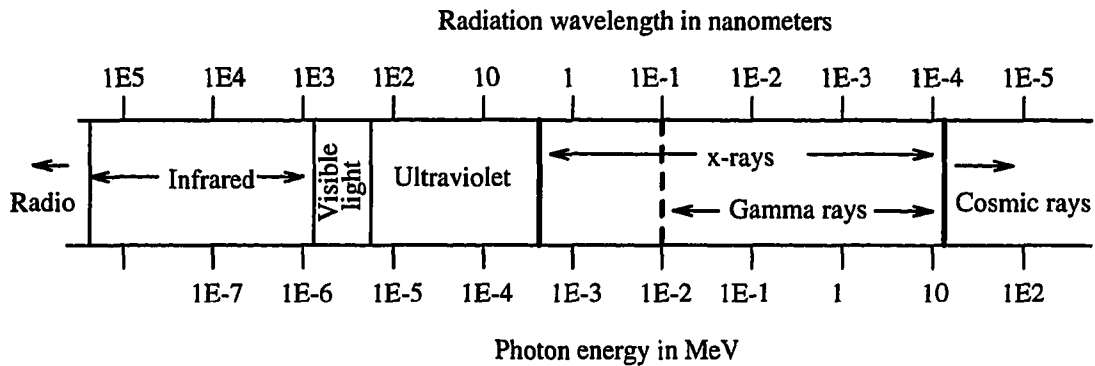


Figure 1.1: The electromagnetic spectrum

soft body tissue but are strongly attenuated by bone, x-ray photographs can reveal the detailed structure of the human skeletal system and are invaluable in medical diagnostics of broken bones. Similarly in solid materials, it was realized that the attenuation of x-rays is less along paths where there is a cavity in the specimen and industrial radiographs were taken as early as 1896 [17]. Since that time, radiography has vastly expanded to include different sources and types of penetrating radiation along with their recording mediums. In the United States, the radiographic profession started in 1922 when the first industrial radiographic laboratory was installed at the Watertown Arsenal by Dr. H. H. Lester, to aid in the development of steel castings for Army ordnance components [3].

Sources of X-ray

As mentioned earlier, x-rays are generated when a beam of high-energy electrons hits a metal target, so the essential elements of an x-ray tube are:

- a filament, as a source of electrons (the cathode).

- a metallic target (the anode).
- a high-voltage supply which can be connected across the cathode and anode.
- high vacuum container.

A modern x-ray tube consists of an insulating, vacuum-tight envelope containing the cathode and the anode. The cathode is a tungsten filament, usually wound spirally, and surrounded by a shaped metal electrode called the focusing cup. This cup, which is usually made of iron and nickel, acts as an electrostatic lens, and controls the shape of the electron beam emitted by the cathode. The size of the focal spot depends on the dimensions of the filament. The anode (target) is usually made of tungsten, but targets made of molybdenum are not uncommon. The voltage applied across the tube controls the energy of the emitted x-ray, while the intensity of the x-ray beam is controlled by the current that passes through the filament. A schematic of a typical modern x-ray device that produces a continuous spectrum of x-rays is shown in Figure 1.2.

When electrical current passes through the filament, the temperature of the tungsten anode increases and eventually electrons start to boil off. Then the high potential accelerates these electrons towards the cathode. As the electrons interact with the target, most of them lose their kinetic energies in numerous collisions with the atomic electrons of the target material. Their energy is transferred into heat. That is why the anodes in x-ray tubes are made of a material with very high melting point like tungsten (or/and sometimes a way of cooling the target material is necessary). A few electrons, though, lose most or all of their energy in single collisions with target atoms generating bremsstrahlung radiation. In this way, many

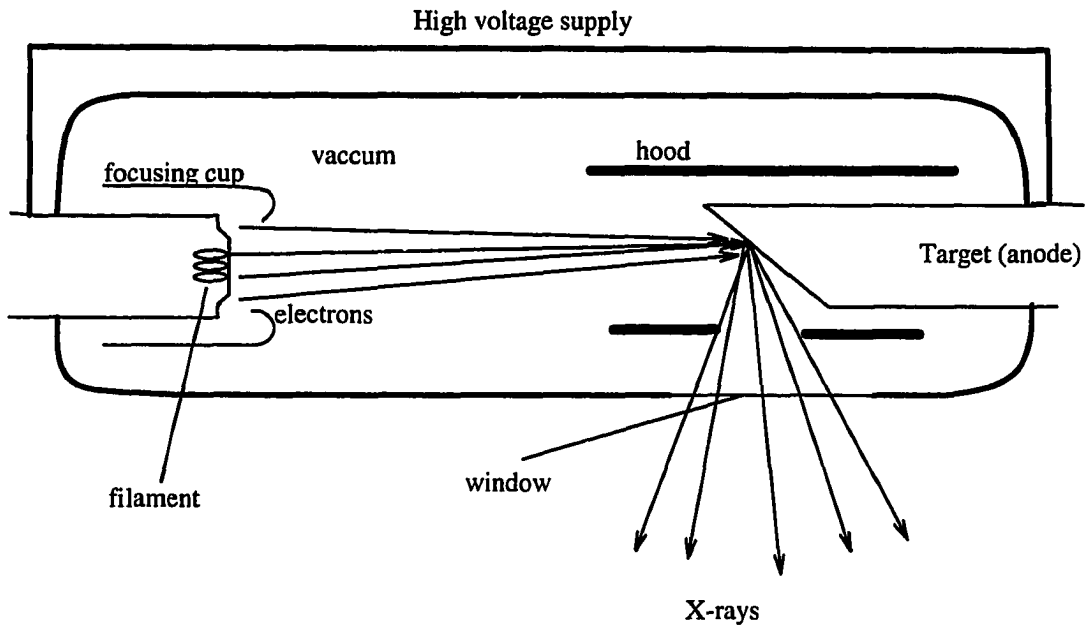


Figure 1.2: A schematic diagram of a typical x-ray generator tube

wavelengths are emitted resulting in a continuous x-ray spectrum. Such an x-ray spectrum is sometimes referred to as “white x-ray spectrum”. The maximum energy that a photon may have is when there is a complete conversion of all the kinetic energy of an electron into a bremsstrahlung photon. In this case the photon has a wavelength of:

$$\lambda_{min} = \frac{hc}{V} = \frac{12395}{V} \text{ \AA} \quad (1.1)$$

where h is Planck’s constant (6.626×10^{-34} joule seconds), c is the speed of light (2.998×10^8 m/sec), and V is the tube voltage. This will be the maximum energy of the continuous energy spectrum and it equals the voltage applied to accelerate the incident electron beam.

A typical x-ray spectrum looks like Figure 1.3. The high intensity narrow peaks in the spectra are called *characteristic x-rays*. These characteristic peaks are superimposed on the continuous bremsstrahlung spectrum, and they appear only when the energy of the incident electron exceeds the ionization energy of the levels of the atomic electron cloud. The characteristic x-ray peaks correspond to the transition of atomic electrons between different energy shells. When an electron from the K-shell for example is knocked out, another electron from the outer energy shells falls back to fill the hole in the K-shell. In this transition, the atom emits a quantum of electromagnetic radiations with an energy equal to the difference in the energy levels between the two shells. In the more likely case, when the electron drops from the L shell, the K_{α} peaks result, and when the dropping electron is from the M shell, the smaller K_{β} peaks results. Both K_{α} and K_{β} split into two lines because of the electron spins in the K shell.

Since the energy differences between energy shells is unique for each element, the energies at which these high intensity peaks occur is different for each target material, and hence the name *characteristic*. Figure 1.3 shows that the characteristic peaks of the K_{α} for tungsten are at 57.98 keV and 59.3 keV for the spin up and spin down K electrons respectively.

Another source of penetrating radiation is the decay of radioactive isotopes from which a monoenergetic beam of photons is emitted. These isotopes have an important advantage over x-ray generators due to the fact that they are highly portable. Manufactured radioactive isotopes can easily be transported to areas where x-ray tubes are difficult to handle or are too bulky. The isotopes that have the widest use are ^{192}Ir and ^{60}Co [5]. The radiation of these two isotopes are used to penetrate

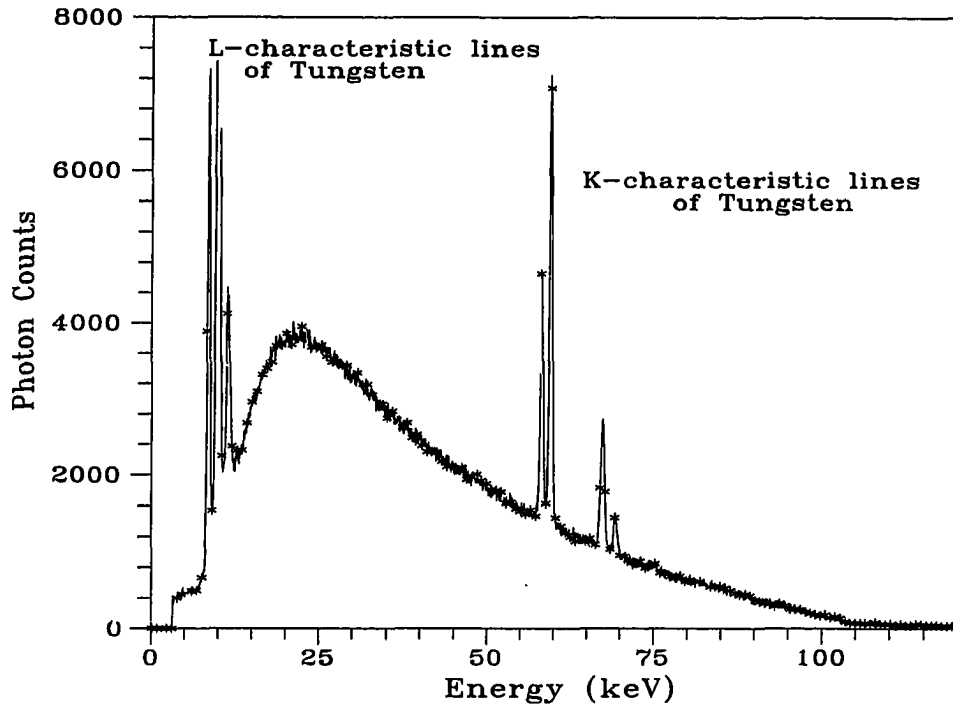


Figure 1.3: A typical x-ray white spectrum

carbon and stainless steel from about 12 to 200 mm in thickness, covering much of the pipe, casting, and vessel wall thicknesses commonly manufactured. The ^{192}Ir has a penetration effectiveness of an x-ray tube with a peak energy output of approximately 900 keV. The down side of using this isotope is its 74 days half life, which means that the exposure time must be increased 7 percent each week. The source is usually replaced when the decrease in strength makes the longer exposure time uneconomical. High intensity radioactive isotopes like ^{192}Ir and ^{60}Co are usually shielded with depleted uranium.

Nondestructive Evaluation

Nondestructive evaluation (NDE) is the art and science of examining assemblies and system components without compromising their integrity. There are several major methods for NDE: radiography, ultrasonics, magnetic, electrical, penetrant, acoustic emission methods, thermography ...etc. Many of these techniques have reached a stage of development where a semi-skilled operator can use the technique efficiently without the need to understand the physical principles behind the technique. However, understanding the physics and the technical details of a nondestructive testing technique is essential for the designer before specifying a certain inspection technique. It is also important for the development engineers working on new methods to have a thorough scientific understanding of the physics involved in a specific technique, its capabilities and its limitations before they can improve on it.

Applications of NDE include flaw detection in materials like weld defects and lack of bond in adhesive joints, fatigue cracks developed during service. Other important applications include the examination of assemblies, the detection miss-assembled components, missing or displaced parts, measurement of spacings, etc. However, for an effective application of a certain NDE technique, its capabilities must be considered early in the product's design phase.

Simulation models of NDE techniques are cost-efficient and time saving tools that have proved to be helpful in understanding how these techniques work. It is also cost and time saving to predict the result of an NDE inspection without having to actually do the inspection. This will give the user a chance to adjust the inspection parameters to achieve the desired result. Once optimal settings for the different parameters have been reached, the actual inspection can be carried out.

NDE simulation models can be used to select the optimum inspection technique for a certain specimen. Sometimes, more than one NDE technique can be used to conduct a certain inspection. Depending on the specifics of the situation, some techniques are more appropriate than others. For example, in weld inspection, x-rays are commonly used to detect inclusions from a tungsten welding electrode where the tungsten attenuates almost all of the radiation passing through the weld and shows almost an unexposed area on the radiograph. On the other hand, porosity, incomplete penetration, and lack of fusion are seen as areas of less thickness, permitting more radiation to go through the specimen. However, the detection of cracks in weldments, castings and other fabrications is highly dependent on their orientation, depth, and width. These characteristics of particular types of discontinuities determine the nondestructive tests to be applied. A combination of methods or techniques may be necessary to assure a structure's satisfactory performance. In a pipe weld, for example, it may be necessary to use radiographic, ultrasonic, and magnetic particle test methods to determine that all discontinuities of a certain size, both surface and internal are detected. The ability of the x-ray technique to detect cracks depends very much on the crack opening and its angle to the radiation beam. Ultrasonic NDE can be most appropriate and more reliable in cases where the crack is a planar opening between the weld layers, yet x-ray radiography is used more often for pipe weld inspection [6]. Simulation models are needed to select the appropriate NDT inspection method(s) to assure that no major discontinuities can go undetected.

Integrating NDE techniques into the design process is a new approach that combines the inspectability of the product using NDE techniques with the other aspects of the design process [7]. NDE models can provide an easy and inexpensive way to

obtain the necessary information about the inspectability of the part and the appropriate inspection method. Integrating the minimum detectable flaw size predicted by NDE models, with the stress and materials analysis in the design stage, will enable the designer to more accurately control the life expectancy of the product. The designer can then make the necessary changes in the design (materials, manufacturing...etc) to insure that the minimum detectable flaw size is smaller than the critical size at which a catastrophic failure might occur. This way NDE techniques can prevent catastrophic failures by detecting flaws before they propagate to the critical size.

Radiography

A radiograph is a photographic image produced by a beam of penetrating ionizing radiation after passing through a specimen, and radiography is the production of radiographs [17]. In radiography, a source of penetrating radiation (x-rays for example) is incident on one side of a sample and a detector is placed on the other side. When passing through a certain specimen, proportions of the radiation are absorbed as a function of the thickness, material of the specimen, and energy of the incident radiation. More radiation will be absorbed in the thicker parts of the specimen than in the thinner parts. When the radiation hits an x-ray film behind the specimen, the effect of thickness variation will be reflected in a corresponding variation in the optical density on the film. Thin parts will look darker on the film than thick parts. The variation in the specimen thickness might be due to actual thickness variation and it might be due to a void in the specimen or an inclusion. Figure 1.4 shows the basic components necessary in radiography, a source of penetrating radiation, a specimen, and a detector. The source of penetrating radiation could be a nuclear reactor, a

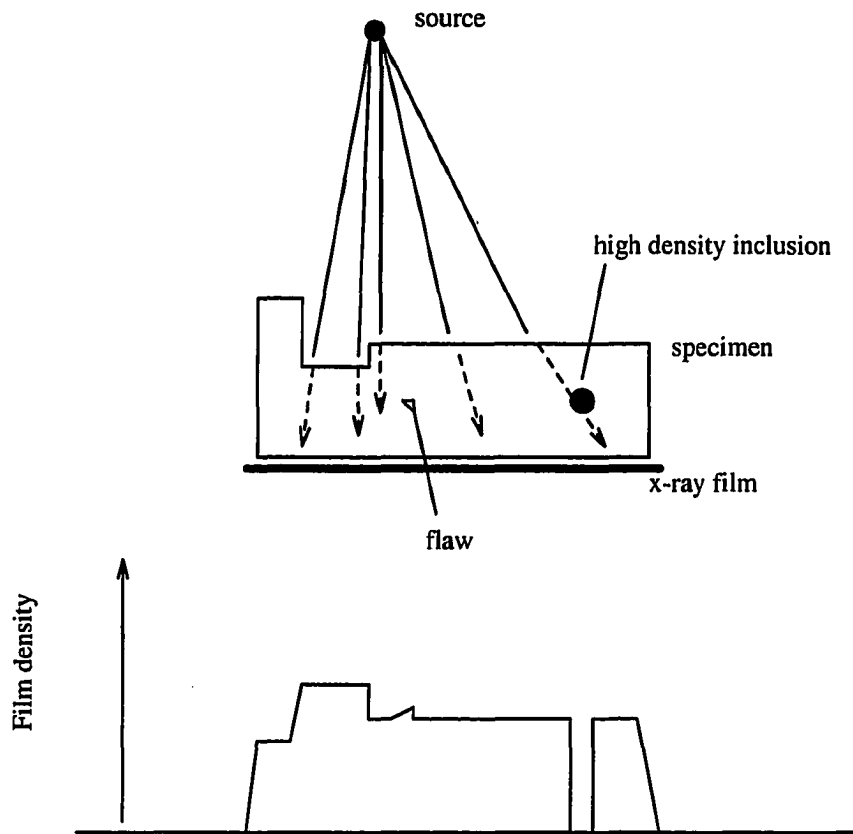


Figure 1.4: The radiographic setup consists of a source, a specimen and a detector.

radioactive isotope, an x-ray generator tube, a linear accelerator ...etc. Similarly, the detector could be a neutron detecting device (usually indium or gadolinium foil), or an x-ray detecting device (x-ray film, HPGe, NaI(Tl),...etc).

Two different types of penetrating radiations are commonly used in radiography, namely neutrons and x-rays. Neutron radiography is appropriate for examining elements that have high thermal neutron absorption cross section. These elements, if arranged in order of increasing atomic number, appear to be random. This is be-

cause, unlike photon attenuation coefficients, the neutron absorption cross sections do not depend on the electron structure of the atom. For low energy neutrons, the absorption cross sections are a $\frac{1}{v}$ curves with resonances superimposed on them (where v is the velocity of the neutron). These resonances are regions of very high cross sections with very small widths and they strongly affect the average absorption cross section in that energy range. These resonances occur in elements when the phase of the wave function of the incident neutron matches that of a nucleon inside the nucleus [8]. This condition is more likely to be met with some elements than others, especially with thermal neutrons. The drawback of neutron radiography is the cost associated with neutron sources. Usually, neutrons are generated in nuclear reactors which means that the inspected object has to be brought to the neutron source. Otherwise, portable neutron sources are extremely expensive in addition to the health risks associated with transporting and operating these sources. X-rays on the other hand, are more sensitive to heavier elements. This is because the interaction of photons with matter occurs mainly between the photons and the atomic electrons. The more atomic electrons, the higher the interaction probability. X-ray sources however, can be made portable and compact but there are still some problems associated with portable sources. In the case where the x-ray source is a radioactive isotope, there are practical limits on the intensities that can be obtained, in addition, there is a risk of accidents while transporting and operating with high intensity radioactive isotopes. The other case where the photon source is an x-ray tube, the size of the source and the associated equipment, especially the power supply, is a major drawback. In any case there are health concerns when working with penetrating radiations. This means that the source of radiations has to be shielded when radiations are emitted

or a certain area has to be evacuated. Luckily when x-ray tubes are the source of photons, radiations are emitted only when the machine is turned on. This minimizes the health risks and restricts the need to shield the x-ray source (or to evacuate the area) to only when the machine is in use.

Generally speaking neutron radiography is a complementary technique to x-ray radiography. Neutrons are usually used in situations where it is not easy to see with x-rays. These situations arise when we are interested in differentiating between two light materials or when a light material is hidden behind a strong photon attenuating medium. Examples of applications of neutrons in NDE include oil well logging where the neutron scattering by hydrogen is so high relative to the surrounding materials. Neutrons are also used to trace the flow of lubricating oil in engines where a light photon scatterer (oil) is shielded behind a strong attenuating medium, cast iron in this case.

Radiography has been used in nondestructive testing since the discovery of x-rays. Since then, the role of radiographic inspection has played an important role in assuring product quality by allowing manufacturers to detect small flaws and defects within the volume of the object. It is also a valuable technique used in the search for better materials and improved manufacturing processes. X-rays have found a wide-spread use in NDE applications like:

1. Weld radiography: X-ray radiography is widely used in weld inspection. Both surface and internal defects in the weld can be shown on the radiograph. This method of inspection has been the accepted one in the U.S. Navy since the 1940's. Ultrasonics inspection of welds was accepted in the Navy to inspect welds that are not accessible for radiography [6]. Pipe welding is an impor-

tant application for x-ray radiography, where a full 100% inspection is usually required. Pipelines are fabricated by butt-welding lengths of pipe, using 360° circumferential butt-welds. Pipes vary from 48 inch diameter down to 6 inches and even to 1 inch for chemical plants. Consequently there are several x-ray radiography inspection methods each is more appropriate for a specific situation than the other methods [17].

2. Casting radiography: Radiography with film as its recording medium, is one of the most effective NDT methods for quality control of castings. Radiography of castings indicates the quality of the product within the limits of the inspection method. This method of inspection is particularly effective for discontinuities which displace a volume of cast material.
 3. Crack and inclusion inspection: Small cracks and inclusions are points of stress concentration which can eventually propagate and cause component failure. The ability to detect a crack depends very much on the crack opening and its angle to the incident x-ray beam. Generally speaking, x-ray film radiography can reach sensitivities up to less than 2% of the thickness. Sensitivities obtained from a real time x-ray inspection using image intensifiers can reach 5% of the thickness.
 4. Corrosion detection: Corrosion products have lower attenuation coefficients for x-rays than the original metals. Hence, comparing the transmitted radiation through the corroded spot at two different energies of the incident radiation makes it possible to quantify the amount of metal lost due to corrosion [12].
 5. Assemblies radiography: Assemblies such as jet engines, gas turbines, valves,
-

nuclear fuel elements and explosive devices (bombs and fuses) are frequently radiographed with high-energy x-rays to show internal conditions or dimensions.

6. K-edge detection of contaminants: This application depends on a process similar to the process that causes the emission of the characteristic x-ray. A beam of electrons might interact with the atomic electrons and eject electrons from the k shell. Electrons from higher energy shells will fill in the hole and a quantum of electromagnetic radiation with energy equal to the difference between the energies of the two shells is emitted. By the same sense, incident electromagnetic radiations with energy equal to the energy of the k shell electrons will be preferentially absorbed. Since the energy of the electrons in the k shell is a characteristic of each element, the energy of the absorbed incident beam can be used to identify the type of material that has absorbed the energy. Moreover, the intensity of the absorbed radiations can be used as a measure of the amount of the absorbing material.

 7. Medical applications: As mentioned earlier this was one of the very first applications of x-ray for nondestructive evaluation. X-ray photographs are becoming invaluable in medical diagnostic procedures leading to the resetting of broken bones. Two disadvantages of x-ray photographs limit their usefulness. They are not very effective in differentiating between different types of soft tissue (as in locating tumors for instance), and they produce a flat, two-dimensional image that even if it reveals an abnormality, would not indicate the depth of that abnormality within the body. Moreover, interesting soft tissue can be shielded or obscured by bone, for example the brain within the skull.
-

X-ray Interactions with Matter

There are three main ways in which photons interact with matter. These are *photoelectric effect*, *pair production*, and *Compton scattering*. In the photoelectric effect, the incident photon interacts with the entire atom, the photon disappears, and one of the atomic electrons is ejected from its shell (photoelectron). The energy of the photoelectron equals the energy of the incident photon less the binding energy of the electron. If a photon succeeds in ejecting an inner atomic electron, the hole in the electronic structure is later filled by a transition of one of the outer electrons. This transition is accompanied by the transmission of x-rays characteristic of the atom. The probability for photoelectric absorption is most significant for low-energy photons ($\simeq 100$ keV). It increases rapidly with the atomic number Z of the absorber atoms (roughly as Z^4), and it decreases rapidly with increasing photon energy (roughly as E_γ^{-3}) [8].

Pair production requires that the photon has at least a threshold energy of $1.02MeV$. In this process, the photon disappears and an electron pair (a positron and an electron) is created. The electron moves about and loses its energy due to collisions with atomic electrons in the surrounding media. The positron slows down to a very low energy where it combines with an electron, the two particles disappear, and two photons are produced, the two photons are called the *annihilation radiation*. This type of interaction is only important for photons with very high energies.

Compton effect is simply the inelastic scattering of a photon by an electron in which both energy and momentum are conserved. This type of interaction is the very important in the energy ranges usually encountered in x-ray radiography. As shown in Figure 1.5, the incident photon with energy E'_γ is scattered through the angle

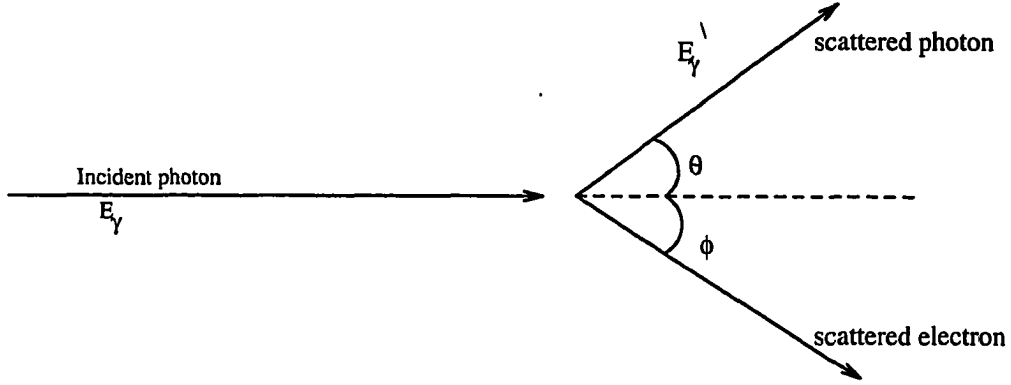


Figure 1.5: Compton effect.

θ and the struck electron recoils. From the conservation of energy and momentum (using relativistic dynamics) gives:

$$\frac{E_\gamma}{c} = \frac{E'_\gamma}{c} \cos \theta + \frac{mc\beta \cos \phi}{\sqrt{1 - \beta^2}} \quad (1.2)$$

$$0 = \frac{E'_\gamma}{c} \sin \theta - \frac{mc\beta \sin \phi}{\sqrt{1 - \beta^2}} \quad (1.3)$$

$$E_\gamma + mc^2 = E'_\gamma + \frac{mc^2}{\sqrt{1 - \beta^2}} \quad (1.4)$$

where E_γ and E'_γ are the incident and scattered photon energies respectively, c is the speed of light in vacuum, m is the rest mass of the electron, and $\beta = \frac{v}{c}$. If we observe the scattered photon, then we eliminate the unobserved variables β and ϕ . The result is Compton-scattering formula:

$$E'_\gamma = \frac{E_\gamma}{1 + (E_\gamma/mc^2)(1 - \cos \theta)} \quad (1.5)$$

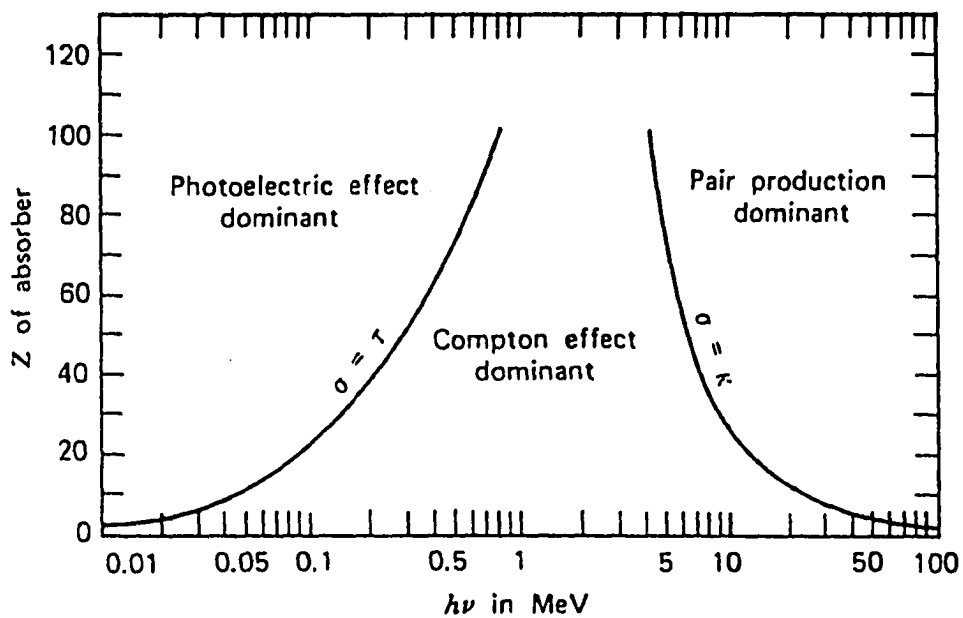


Figure 1.6: The relative importance of the three major types of photon interactions. τ σ κ are the probabilities of a photoelectric event, Compton scattering, and pair production respectively

Figure 1.6 shows the relative importance of the three different photon interactions with matter. The lines show the values of the atomic number and energy for which the two neighboring effects are just equal.

CHAPTER 2. X-RAY RADIOGRAPHY SIMULATION

Introduction

Computer simulation of physical processes is becoming a significant tool in studying these processes especially with the widespread use of powerful and inexpensive digital computers. Using simulation codes to study the effect of different variables on the physical process is a more convenient and cost efficient method than the traditional way of performing laboratory experiments. Computer simulation of NDE techniques has the following advantages:

1. It provides an easy way to predict the detectability of small flaws and inclusions. Accurate simulation of the technique can predict the minimum detectable flaw size while a product is still in the design phase. The probability of detection (POD) (defined as the number of flaw detected by a certain method divided by the total number of flaws [7]) can then be used to ensure a certain level of inspectability of the product while in service. If the POD is not high enough, a change in the inspection method or the component design can be made at an early stage and hence saving cost and effort.
 2. Optimizing the inspection parameters: Large quantities of data can be processed at very high speeds and a simulation code can predict the output of the
-

inspection technique, hence allowing the user to choose appropriate technique parameters and to adjust the equipment to give the desired result. In x-ray radiography for example, the best contrast is obtained by using a low voltage with as long exposure time as the user can tolerate. Several runs of a simulation code can provide the user with the optimum generator settings to get the best contrast for a given inspection time.

3. Optimize the sample orientation with respect to the source and detector: Especially for complex geometries and assemblies, the POD strongly depends on the orientation of the object. Flat surfaces that are not of interest in an assembly can be made to look like a straight line by orienting the assembly on an appropriate angle and hence allowing other important features in the assembly to be seen. The optimum orientation of a complex part or an assembly can be easily obtained by repeating the runs of the code for different object orientations compared to actually doing the inspection several times until the appropriate orientation is obtained.
 4. Unified life cycle engineering [7]: Integrating the NDE inspectability in the designing process for ultimate utilization of the NDE capabilities. NDE requirements must be considered at every stage of a product's design. For example during the material selection stage, the designer should make sure that the selected material is compatible with NDE. When dealing with complex problems, the designer must determine when, during the overall fabrication and assembly process, the NDE controls will be most effective and least expensive. Similarly, during the layout stage, the inspectability of the product must be determined.
-

A critical flaw size is determined based on the material type, geometry and the mechanical and thermal stresses under which the component will be operating. If this critical flaw size is smaller than the minimum flaw size that can be detected using a particular inspection method, then either design or the inspection method can be changed or revised to allow in service NDT of the product. Obviously the NDT is a cost element at this point, but when properly applied it could substantially reduce the total life-cycle cost.

So integrating the NDE simulation models in the design process allows us to determine the most appropriate design or inspection method at each stage of the design process and hence assures the product high quality and in service inspectability.

5. Training: With the high competition in today's market, it is no longer economically feasible to train engineers and technicians by repeating experimental work over and over again. Computer simulations of inspection techniques provides the necessary fast and cost efficient tool for training purposes. Effects of different parameters as well as the limits and resource requirements for a certain inspection can be included in the simulation. This will give the user a qualitative feeling of the capabilities of the technique and a quantitative estimate of the expected output.
 6. Comparison of NDE techniques: Evaluation and comparing the capabilities of different NDE methods requires the fabrication of a set of specimens with different severities of the defect, inspecting them nondestructively and then analyzing the results statistically. With so many different types of defects and so
-

many NDE techniques available, one can imagine how elaborate and exhaustive it is to accumulate enough data to be statistically viable. Simulation models on the other hand, can produce such needed data relatively easily, analyze the data, and compare the capabilities of different NDT methods.

The X-ray Radiography Simulation Code “XRSIM”

There are three distinguishable parts for the simulation of x-ray radiography. These are: the simulation of the x-ray source, the interaction of photons with the examined sample, and finally simulation of the detector response. XRSIM generates a bremsstrahlung spectrum by simulating the basic electron-electron physical interactions [9] [11]. The inputs to this part of the code are the x-ray generator specifications and settings, and the output is a distribution of photon intensity versus energy. Figure 2.1 shows the output of the spectrum obtained from the simulation code compared to that obtained experimentally using HOMX-160 x-ray generator. The simulated spectrum came to within 10% of the actual spectrum (when comparing the areas under the two curves).

Simulation of the interaction of photons with the sample material is the most computationally expensive part of the code. The code uses the linear attenuation coefficients of the sample material to calculate the portion of the incident beam that will pass through the examined object: The formula used is:

$$I(x, y, E) = I_o(E) \int_{source} \frac{e^{-\mu(E)\rho}}{r^2} dA \quad (2.1)$$

where μ is the mass attenuation coefficient of the inspected material, ρ is the thickness of the object, and r is the radial divergent of the beam from the location of the source

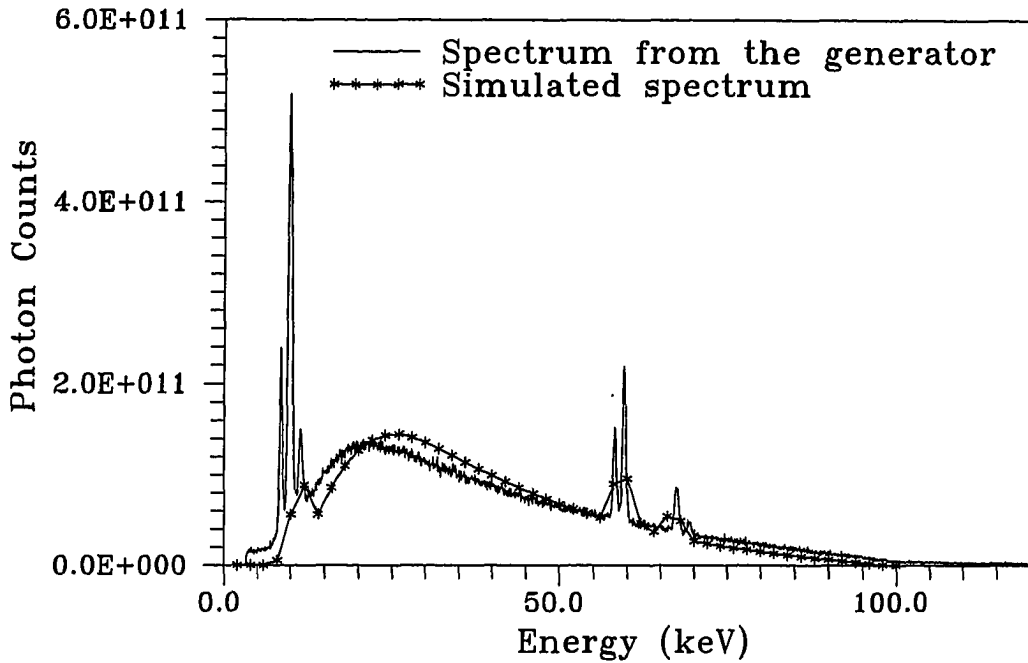


Figure 2.1: The simulated bremsstrahlung spectrum compared to a normalized spectrum obtained from an actual x-ray generator (HOMX-160)

to the pixel at location x and y . The integration is carried over the area of the source (in most cases a point source assumption is valid). A computer aided design “CAD” interface calculates the distance ρ at each pixel using the ray path intersections with the triangular facets representation of the object surface. Then the simulation code reads the thicknesses matrix ρ and uses the photon attenuation coefficients of the object material to calculate the uncollided flux that reaches a film behind the object. The interaction with a CAD interface to convert the surface facet representation of the object into a thickness at each pixel is a unique advantage for XRSIM over any other simulation code, because it removes the limits on the geometrical complexity of the examined sample. The CAD software I-DEAS creates the surface representation of the sample as triangular facets. The CAD interface reads the coordinates of the

vertices of each triangle and calculates the coordinates of intersection between the ray path and the triangular facets. The ray path is the straight line connecting the source and each one of the pixels in the film plane. In addition to simulating a point source, the code has the ability of simulating a finite size source by dividing the source into several point sources and then summing up the contribution of each one of them. Since the bremsstrahlung spectrum has a continuous energy distribution, the code divides the spectrum into a user input number of energy bins. Finally the code converts the photon beam that reaches the film into optical density:

$$D(E) = D_o(1 - e^{-\sigma I(E)t}) \quad (2.2)$$

where D_o is the saturation density of the film, and σ is the efficiency of the film. Figure 2.2 shows an example of the output of XRSIM. It should be noted at this point that the typical execution time of the code to produce a (256 x 256 pixels) image like the one shown in Figure 2.2 is around 30 seconds on a DEC500/240 work station. Figure 2.2 shows that the images generated by XRSIM are different from what we would obtain experimentally. This is partially due to the fact that XRSIM in its current status ignores the contribution of scattered radiation to the final image.

Limitations of XRSIM

In its current form, XRSIM calculates the uncollided photon flux to generate the radiographic image. Although most of the photons that reach the film are usually uncollided, a portion of the photon beam will suffer one or more Compton scattering events before reaching the film. This portion is called the "scattered flux" and its amount depends on the energy of the incident beam, the material type and thickness of the sample. XRSIM assumes that all the photons that are removed from the main

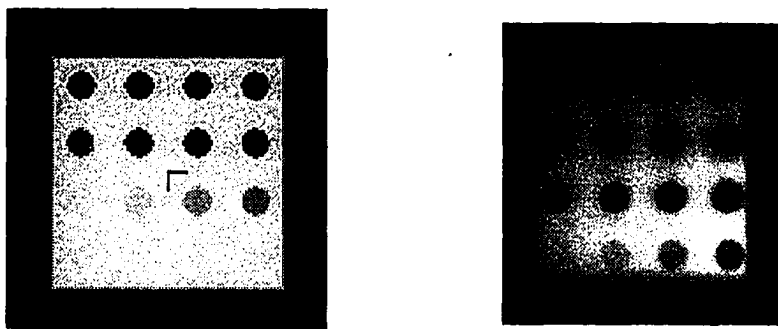


Figure 2.2: A radiographic image of a block of Al with 16 holes of different depths in it generated by XRSIM (left) compared to an image generated experimentally (right)

photon beam never make it to the detector (film). This assumption might be of some validity in situations where the energy used is low (few keV's) and the sample material is of a high Z value. This is because most of the interactions at low energies with heavy materials are photoelectric absorptions, and hence the photon disappears. However, for most applications in industrial radiography, this assumption is far from being valid. The relative importance of the different photon interactions in the energy range of interest to x-ray radiography was shown in Figure 1.6. The Figure shows that at 100 keV and for a material commonly used in radiography like aluminum, the dominant type of interaction is Compton scattering. Actually for this energy and this material, Compton scattering is almost one and a half times as important as the photoelectric effect.

Another type of scattering that is not accounted for in XRSIM is the scattering in the film plane itself. The silver halide grain in the emulsion layer in an x-ray film is activated either via photoelectric absorption or by a Compton scattering event. In the

later case, the photon loses some of its energy and scatters at a certain angle, while the electron recoils and settles in a neighboring site. The scattered photon depending on its new energy and direction, might travel in the film plane and interact with more silver halide grains and hence activate them. The recoiling electron might scatter along the emulsion layer as well, however, the range of charged particles in matter is very small compared to the range of photon. The activation of the silver halide grains due to photon scattering in the film plane is called "film undercut".

Scattering corrections are not the only limitation of XRSIM. For example the code does not handle multiple objects and multiple materials. This feature which has been added to the code but not integrated in the latest version of XRSIM, is especially important when dealing with assemblies. It is not uncommon for the examined specimen to be an assembly made of several parts and each or some of these parts are made of different materials. It is not uncommon for the examined specimen to be an assembly made of several parts and each or some of these parts are made of different materials. Also the code uses only elliptical and conical sections flaw shapes. This is because of the relative simplicity of finding the intersections between these surfaces and the ray path. However, a more realistic flaw shape requires a CAD interface similar to the main CAD interface that handles the main object. Other limitations of XRSIM include its inability to handle rough surfaces and a lack of accuracy in the film noise model.

X-Ray Computer Tomography Simulation Code "CTSIM"

X-ray computed tomography is used to produce an image of a plane in the object without interference from adjacent planes. The image represents the linear

attenuation coefficient of the object. In computed tomography, the image plane is parallel to the beam axis, and the image must be produced by computer techniques. Figure 2.3 shows the scanning and reconstruction process for tomography. The data collected from the detectors eventually ends up as digital data stored in a computer. The computer controls the movement of the scanner, collects the data, applies a reconstruction algorithm and finally displays the resulting image.

The simplest tomographic scanner consists of a collimated source and detector that rotate about the object. This arrangement is very slow but produces the best elimination of scattered radiation. Two other arrangements that are more practical in terms of the data acquisition time are the rotate-rotate type or the third generation type and the rotate-fixed or fourth generation type [10].

In computer tomography, x-ray scattering leads to artifacts in reconstruction because the effect changes with each projection. The significance of the artifacts produced by scattering depends on the path length of each projection, the energy of the incident radiation and the material type of the object. A way to eliminate the effect of scattering is to tightly collimate the detectors, however this option is very difficult to apply in a rotate-fixed type of arrangement. Like XRSIM, the computer tomography simulation code CTSIM calculates the uncollided flux and has no means of accounting for the scattering contribution.

X-ray Scattering Simulation

Several x-ray NDE techniques have been simulated without accounting for the scattering of photons. To make these simulations codes more realistic, a computationally efficient method to simulate photons scattering is needed.

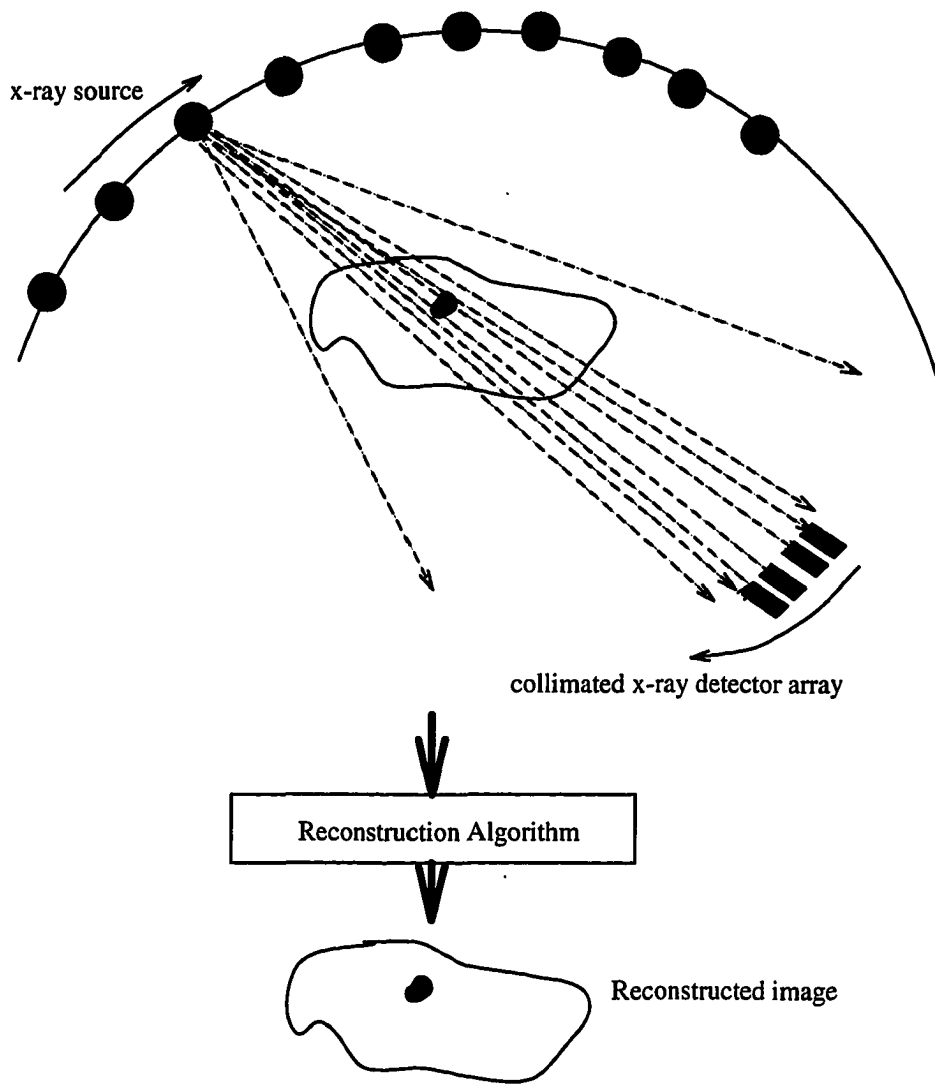


Figure 2.3: Tomographic configuration

To study the scattering of photons in typical geometries usually encountered in NDE applications, we had to develop a new Monte Carlo code that has the ability to interact with a CAD interface to handle complex geometries. Existing Monte Carlo codes require the user to define the geometry of the object as a set of interacting surfaces, and this can be difficult and time consuming process. The Monte Carlo code that we have developed requires the user to generate a CAD model of the object. Then the Monte Carlo code reads the output of the CAD model and translates the surface representation of the object into a thickness array. This feature removes any difficulty the user might face when dealing with complex geometries. This approach to handle scattering was found to be computationally expensive and inappropriate for simulation of NDE techniques where an execution time in the order of few minutes is desired. A more suitable approach but less accurate is to use the concept of buildup factors. This concept has been used before for high energy monoenergetic photons. In this project, intensive experimental and simulation work has been conducted to stretch the definition of buildup factors to accommodate a white spectrum of x-rays at low energies like the ones usually encountered in industrial radiography.

The scattering limitation of XRSIM and CTSIM was the motivation for this work. Previously, an attempt was made to handle the scattering contribution to the radiographic image by solving the Boltzmann transport equation for photons [13]. The execution times obtained using this approach were too long for practical radiography applications. Although studying the scattering of photons in the object was the motivation for this work, we have also studied the scattering of photons in the x-ray film plane itself and evaluated its effect on the film undercut phenomenon. We have also studied Compton backscattering and its use as an NDE technique. This

includes the effect of the different parameters on the magnitude and shape of the backscattered beam. In the next three chapters I will address the scattering in the object, in the film plane, and the backscattering respectively.

CHAPTER 3. SCATTERING IN THE OBJECT

Introduction

When photons strike an object, a portion of the radiation is absorbed and another portion, the uncollided flux, passes through without interacting with the absorber. The intensity variation in the uncollided flux from area to area in the specimen forms the useful image in a radiograph. However, not all the radiation is either completely absorbed and removed from the original beam or transmitted without colliding. Some is deviated within the specimen from its original direction, that is, it is scattered. Scattered radiation contribution to the generated radiographic image depends on the energy of the incident radiation, the object material and thickness. Accounting for the contribution of scattered radiation is very important to obtain a realistic radiography simulation. The energies and materials commonly used in industrial radiography make the contribution of scattered radiation very significant. This scattering contribution is a source of image quality degradation and its effect is noticeable in certain materials more than others.

Photons that suffer a Compton scattering in the sample material, wander around in the object before they either get absorbed, suffer another scattering, or exit the object. In the case when these scattered photons exit the object in the direction of the detector (film), they deposit their energies on the film and hence contribute to the

formation of the radiographic image. For an object with uniform thickness, scattering will increase the resulting film density by a constant amount. This constant amount depends on the energy of the incident radiation, the thickness and the material type of the sample. For a certain energy of the incident radiation, the scattering contribution can be insignificant, equally important, or more important than the uncollided flux contribution. Figure 3.1 shows the relative importance of the scattered radiation and the uncollided radiation (primary) for iron at two different tube voltages. Notice that at 100 kv tube voltage, most of the photons that reach the film are uncollided. Those which scatter lose part of their energy and become more vulnerable for photoelectric absorption. As the tube voltage increases to 200 kv, the population of photons in the energy range where Compton scattering is the dominant interaction mode increases and hence the relative importance of the scattered radiation contribution to the film density increases. It is important to realize that the relative importance of scattered radiation does not necessarily increase as we increase the tube voltage. Depending on the density of the material, at a certain energy most of the photons will go through without interacting and hence reduce the importance of scattering contribution. This phenomena is illustrated in Figure 3.2 where the material has been replaced with aluminum instead of iron. At a tube voltage of 100 kv the contribution from both fluxes is equally important at aluminum thickness of 6 cm. The thickness at which this cross over point occurs differs from one material to another and from a certain tube voltage to another. As indicated in Figure 3.1 there is no cross over point for iron at the tube voltages used in generating these plots. As the tube voltage is increased to 160 kv, the importance of scattered radiation in aluminum decreases because photons with very low energies get absorbed and those with high energies go

through the object without interacting. Although for a 4 cm thick block of aluminum, the number of scattered photons that reach the film when the tube voltage is 160 kv is greater than the number that reach the film when the tube voltage is 100 kv, the relative importance of the second is higher. For iron the number of scattered photons and their relative importance go in the same direction for the energies used in generating Figure 3.1. In both Figures 3.1 and 3.2, the number of photons that make it to the film decreases as the block thickness increases, and hence the error margins increase.

The final radiographic image is a superposition of the effects of uncollided and scattered fluxes. The uncollided flux contribution to the image can be estimated using the attenuation coefficients of the materials used in the radiography. The scattered flux influence can be accounted for by using the Monte Carlo method or by solving Boltzmann transport equation for photons [13]. These two approaches are computationally expensive and were found to be impractical to be used in the simulation of x-ray radiography. Another way to account for the scattering contribution is the use of "exposure buildup factors" approximation. This is a computationally very efficient method, and can be easily integrated in simulation codes. This method depends on using the relatively easier to calculate, uncollided flux to predict the total flux that reaches the film.

Studies to estimate the contribution of scattered radiation to the final image were conducted for the medical applications of x-rays [14] [15]. In these studies the scatterer material were polystyrene and water phantoms in order to emulate the human chest. The scattering contributions to the final image were measured under different exposure conditions. However, only phantoms emulating the human chest were

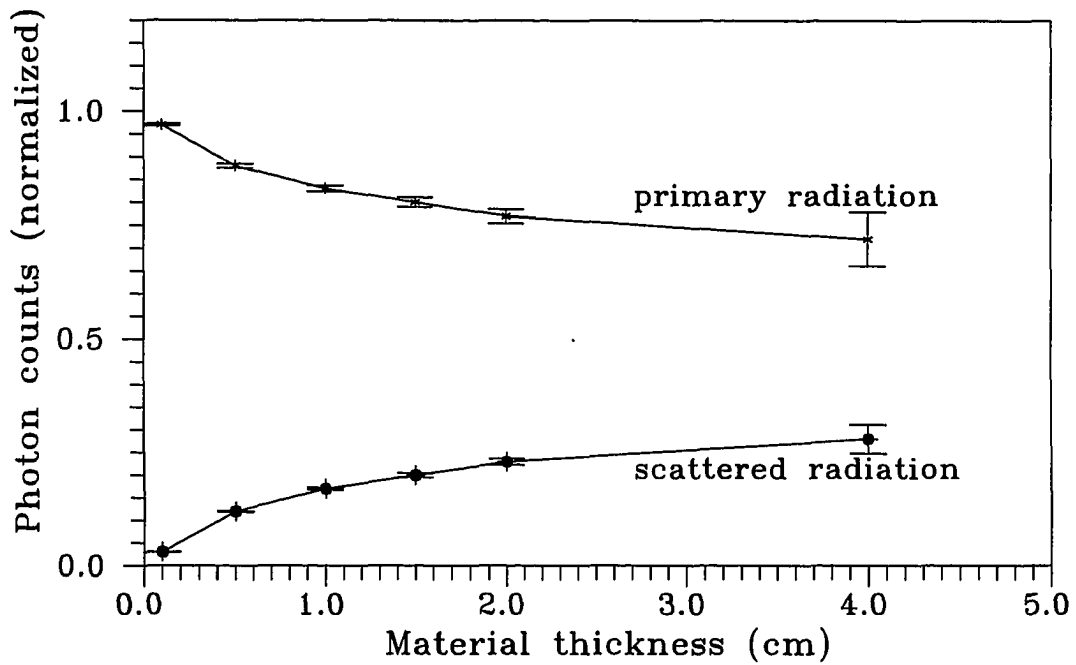
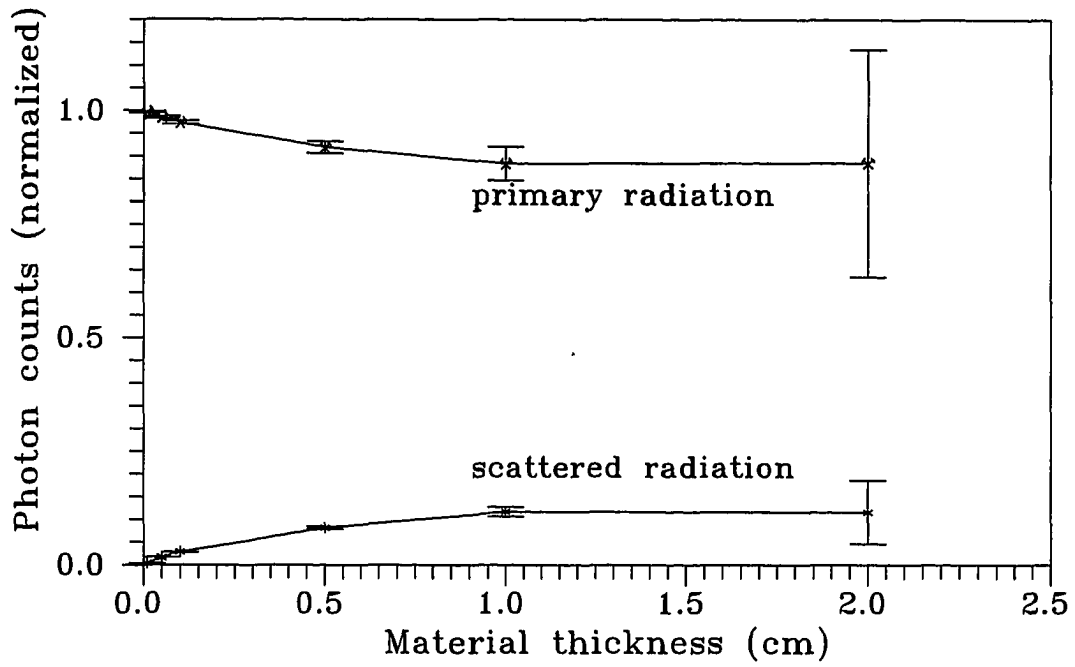


Figure 3.1: Simulated primary and scattered fluxes emerging from a rectangular iron block at 100 kv (top) and 200 kv (bottom) as a function of the block thickness.

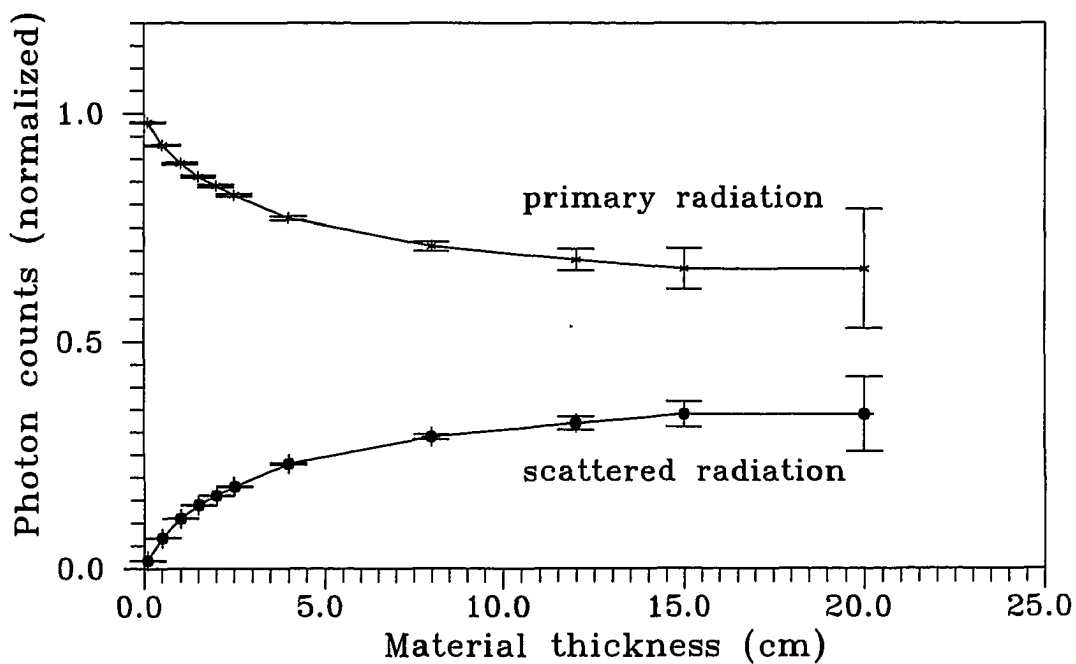
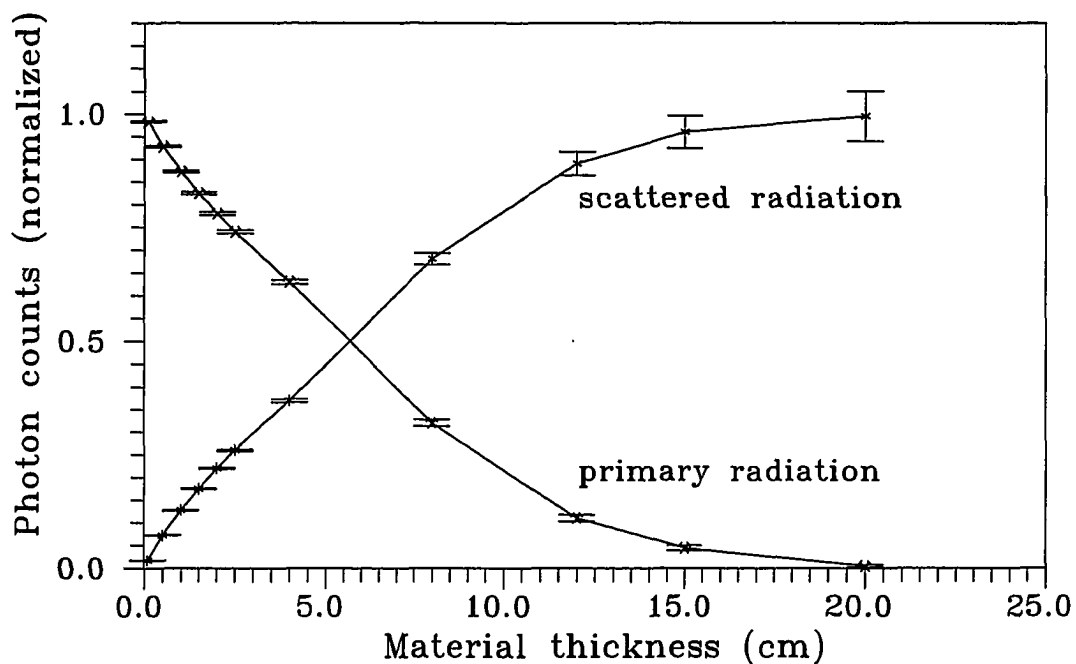


Figure 3.2: Simulated primary and scattered fluxes emerging from a rectangular aluminum block with a tube voltage of 100 kv (top) and 160 kv (bottom) as a function of the block thickness.

used in these studies and with thicknesses typical of a human body. Michitaka has developed an empirical formula based on experimental data to predict the scattered intensity from exposure conditions. The empirical formula estimated the scattered radiation intensity to within 10% using predetermined parameters [15]. This formula however, was developed specifically for phantoms with thicknesses appropriate to emulate the human chest. This restriction on the material type and thickness made the results specific for applications in the medical field. If this restriction is removed, a simple formula to predict the scattered radiation intensity for any material at any thickness will be very difficult.

Buildup Factors

Definition of Buildup Factors

Suppose that the total detector response R_t to both uncollided and scattered photons and the detector response to uncollided photons R_u were known, either on the basis of experimental data or through some accurate calculations. The ratio of the total to uncollided responses, R_t/R_u , is called the *buildup factor* and is denoted by the symbol B . Figure 3.3 shows a plane slab, made of a certain material, with a broad, parallel, monoenergetic beam of photons incident on one face and a detector positioned at the opposite face. The detector response to the uncollided flux alone is:

$$R_u(x) = R e^{-\mu x}, \quad (3.1)$$

where R is the detector response in the absence of the slab, μ is the linear attenuation coefficient of the slab material, and x is the slab thickness. If $R_t(x)$ is the total

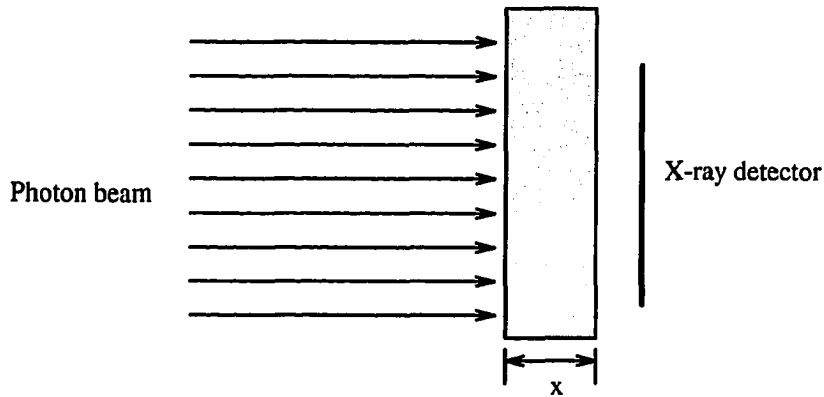


Figure 3.3: Configuration for which the detector response for a parallel beam of x-rays can be predicted using buildup factors

detector response (to both uncollided and scattered photons), the buildup factor B is again defined as the ratio $R_t(x)/R_u(x)$; thus, equation 3.1 is modified to give the total detector response:

$$R_t(x) = R_u e^{-\mu x} B(x). \quad (3.2)$$

Substituting equation 3.1 into equation 3.2:

$$R_t = B(x)R_u, \quad (3.3)$$

and because of the relative ease of calculating R_u in most practical cases, we can easily find the total detector response if only we are fortunate enough to have data for the buildup factors for the situation under consideration.

The response to the scattered radiation can be seen as the difference between the total response and the response to uncollided photons:

$$R_s = R_t - R_u. \quad (3.4)$$

Substituting for R_t from equation 3.3 into 3.4 gives:

$$R_s = (B - 1)R_u. \quad (3.5)$$

The above equation indicates that B can never be less than unity. B can be exactly equal to unity when the circumstances are such that there are no scattered radiations reaching the detector. This situation occurs when the slab thickness in Figure 3.3 equals zero. It should be noted that the buildup factors derived above were defined for monoenergetic radiations illuminating a slab of a certain material of thickness x. Each one of these parameters affect the resulting buildup factor differently. Details of the effect of each of these parameters will be explored later in this chapter.

Buildup factors have been traditionally used in nuclear materials shielding calculations. The radiation sources in these situations are the fissioning nuclei or the decaying radioactive fission products. The radiation emitted in these processes are monoenergetic and consequently the buildup factors were defined for monoenergetic sources. Moreover, the energies at which these factors were calculated are much higher than what is usually used for radiography [16]. In x-ray radiography on the other hand, we usually use a white spectrum source with energies in the range of few hundreds of kilo electron volts. In order to use exposure buildup factors to account for the scattering contribution to radiographic images, we need to introduce a new set of those factors. The new factors will account for the scattering of the whole white spectrum. For an experimental setup where the source is a point source far enough away from the x-ray film that the radiation incident upon it is roughly parallel and uniformly illuminates the film, buildup are functions of:

1. X-ray tube voltage: For each tube voltage setting, the energy distribution of the

bremstrahlung spectrum is different and hence the values of buildup factors will differ accordingly.

2. The type of medium, expressed in terms of the atomic charge number Z for elemental sample materials. For compounds or mixtures a weighted average is usually used.
3. Distance of penetration through the attenuating medium. For monoenergetic sources this is usually taken as the number of mean free path lengths $\mu_0 x$. This is useful because it eliminates the effect of density variations, however for a white spectrum of x-ray tube there is no one single mean free path (mfp) that can be defined and buildup factors are considered to vary according to linear distances.
4. The detector response function. Each film type has a characteristic efficiency for converting the incident radiation to optical density. For this work I have used KODAK-AA x-ray films.

The list above implies the possibility of an enormous number of possible cases and huge tables of resulting data. However reasonable assumptions about the experimental configuration and the energy usually used in x-ray radiography will narrow down the needed cases. Also the types of materials and thicknesses of interest in industrial radiography will further reduce the amount of data needed.

The XRSIM code will calculate the detector response to the uncollided flux. Then using the sample material, thickness, and the x-ray tube voltage, it will access a look up table to find the value of an appropriate buildup factor. The final density (total response) is the density due to the uncollided flux multiplied by an appropriate

buildup factor:

$$D = B(X, kvp, \text{ and material type}) * D_0(1 - e^{-\sigma I_u(E)t}) \quad (3.6)$$

Buildup factors are usually calculated by solving the photon transport equation or by using Monte Carlo techniques. However since we are introducing a new set of factors that will correct for the scattered radiation from a bremsstrahlung spectrum and not from a monoenergetic beam, we chose to rely on experimental work to measure these factors first. However, for the purpose of producing tables of these factors we have developed a Monte Carlo code to reproduce the measured values and to extrapolate the experimental results to other materials and other tube voltages.

Experimental Procedures

Consistency is the key when doing any work with x-ray film development. Consistency in:

1. Film development procedure: The time for each of the film development steps should be kept the same. The resulting film density depends on how long the film is placed in the developer. The longer the time the higher the density, up until the maximum density attainable for that particular exposure
 2. How often the solutions are replenished: It is very important to have fresh solutions at all times in order to obtain reproduceable results
 3. Using identical x-ray films
 4. Uniform temperature of the developer and the fixer used
-

During the experimental procedures listed below, the film was placed in a “Kodak GBX developer and replenisher” developer solution for seven minutes, then five minutes in a “Kodak rapid fix” fixer solution and then washed with water for five more minutes. An alarm clock was used to time for each one of these steps. Solutions were replenished after every 10 films developed, and KODAK-AA films were used throughout all the experiments.

The experimental procedure for measuring buildup factors for a white spectrum of photons consists of the following steps:

1. Find the detector response function (density-exposure curve): The detector response function is a relationship between the energy deposited on the film and the resulting film optical density. When photons fall upon the emulsion, extremely small particles in the silver halide crystals are converted into metallic silver. The number of silver particles formed is proportional to the amount of energy deposited on the film. When the film is placed in the developer, the exposed silver halide grains are differentially attacked [17]. Grains which have received a high exposure are reduced quickly while those which received slight exposure are reduced or developed slowly. Once initiated the development of the individual grain continues until all the silver halide is reduced to metallic silver.

The term “exposure” (not to be confused with the exposure time) is used to measure the effect of photons on a body at any point. This effect is proportional to the number of ions produced in the air at a point outside the body [18]. The number of ions produced is an indirect measure of the amount of energy deposited in the body/film. The unit of exposure is *roentgen*, abbreviated R,

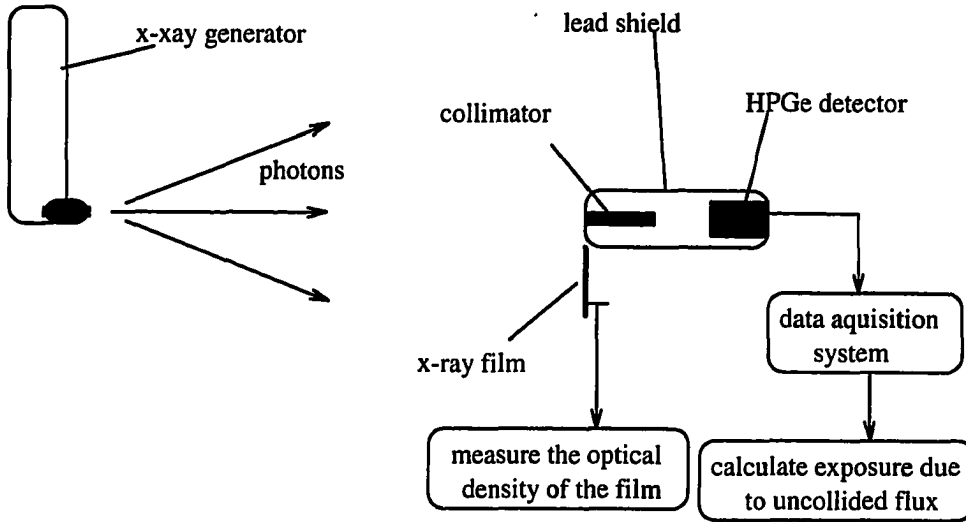


Figure 3.4: Experimental setup for film calibration

which is defined as the production of 1 electrostatic unit of charge of one sign from the interaction of photons in 1 cm^3 of air at atmospheric pressure at 0°C . The exposure “X” is given by the following expression:

$$X = 1.83 * 10^{-8} \sum_i \Phi_i E_i \left(\frac{\mu_a}{\rho}\right)_i^{air} mR \quad (3.7)$$

in this equation, the x-ray fluence Φ must be expressed in $photons/cm^2$, E_i is the photon energy bin in keV, and $\left(\frac{\mu_a}{\rho}\right)_i^{air}$ is the mass absorption coefficient of air at the incident energy E_i in units of cm^2/g . To get the total exposure, the summation in the above equation must be carried for all the energy bins in the x-ray spectrum [18].

As shown in the experimental setup in Figure 3.4, the x-ray white spectrum that went through the collimator can be detected using the high purity germanium (HPGe) detector and then divided into discrete energy bins using a

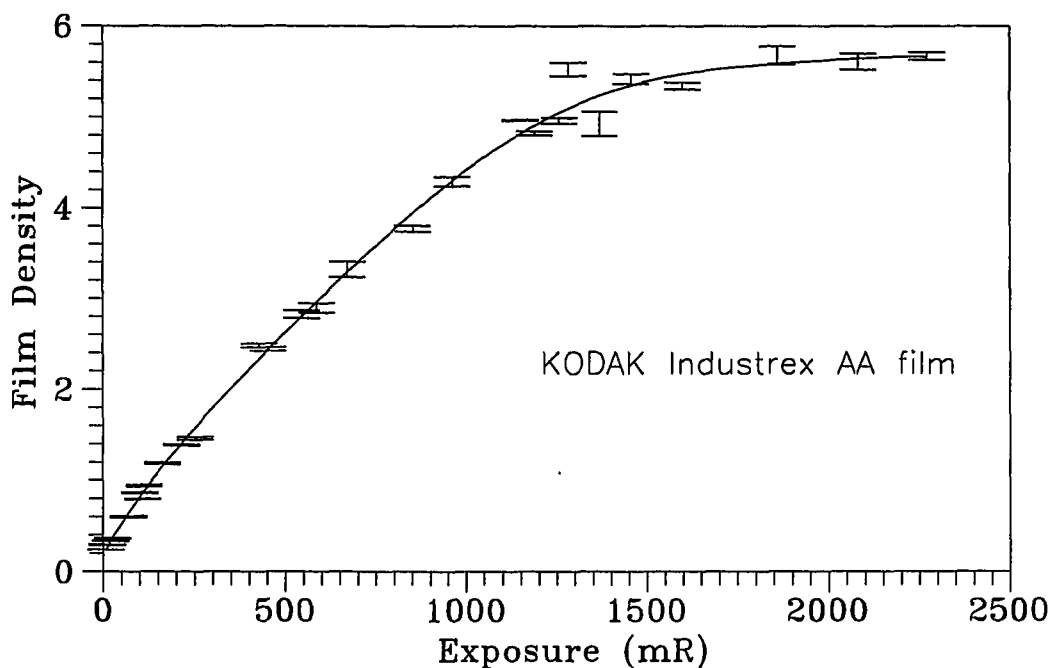


Figure 3.5: Calibration curve for the KODAK-AA x-ray film at a tube voltage of 100 kv

multi-channel analyzer (MCA). The whole data acquisition system is controlled via a personal computer and the output is a list of energy bins and their corresponding photons fluence. Equation 3.7 is then used to integrate over the energy bins and to calculate the resulting exposure. At the same time, the corresponding optical film density is measured directly by developing the x-ray film and using a digital densitometer.

The resulting curves should relate the exposure due to the white spectrum to the film optical density. The process was repeated for several exposures and an example of the calibration curves is shown in Figure 3.5.

The error bars in Figure 3.5 represent one standard deviation from the mean value of four measures across the film for the same exposure. The curve has a linear portion for low exposures before it reaches a saturation level. For an unexposed emulsion, there are such a large number of unactivated grains that the number of grains hit in a relatively short exposure will be proportional to the exposure (energy deposited). Until an appreciable number of grains have been hit the rate of activation of grains will be linear [4]. Beyond the linear portion of the curve is the saturation part where the number of grains available for activation is relatively low and the film approaches its maximum attainable density.

2. The next step is to actually measure buildup factors: Place a plate of the material of interest (say aluminum) in front of the x-ray film and the HPGe detector as shown in the experimental setup in Figure 3.6. Irradiate the plate at a certain voltage. Photons that go through the aluminum plate and into the collimator are the uncollided flux. This portion of the flux will be registered in the same way as in step 1 where the output is the value of the exposure due to the uncollided flux. At the same time, the resulting optical film density is due to the total flux "uncollided + scattered".
 3. The optical density that corresponds to the exposure due to the uncollided flux generated in step 2 is obtained from the film characterization curve, while the optical density that corresponds to the exposure due to both the uncollided and the scattered fluxes can be measured directly from the film exposed in step 2.
-

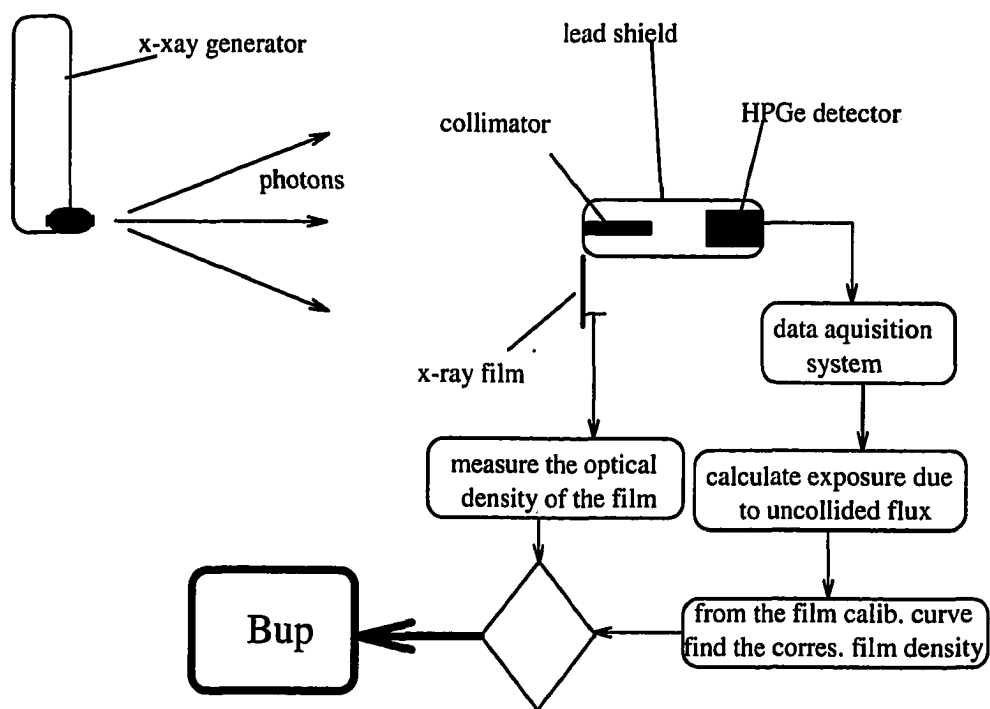


Figure 3.6: Experimental setup for measuring “exposure buildup factors”

Define the “exposure buildup factor” as:

$$B(\text{energy, material type and thickness}) = \frac{\text{total exposure}}{\text{uncollided exposure}} \quad (3.8)$$

This is the buildup factor for aluminum at this particular plate thickness when exposed to a white x-ray spectrum with a maximum energy of 100 keV.

4. Repeat steps 2 and 3 for other aluminum thicknesses (say 0.5, 0.75, 1.0, 2.0 inches). This will generate buildup factors for aluminum at different thicknesses for a white spectrum of x-rays at a maximum energy of 100 keV.
5. Repeat steps 2, 3, and 4 for other voltage settings of the x-ray generator.
6. Repeat the experiment for other materials.

Calculating Exposure Buildup Factors

The experimental procedure described above is very exhaustive and time consuming especially because it has to be repeated several times to achieve consistency in the outcome and also to obtain statistically viable data. It was necessary to do the experimental work to have a basis for tuning up a computer code that calculates exposure buildup factors.

Calculating buildup factors is relatively fast, cheap, and more convenient than measuring them. To do so, we have developed a Monte Carlo code that simulates the two most important photon-matter interactions in the energy range of interest for x-ray radiography, namely the photoelectric absorption and Compton scattering. The code can generate useful information like: the photon spectrum before and after the photons interact with the material, the exposures due to both the uncollided and

the scattered fluxes, the number of photons that interacted with the sample and the number of those that went through it without interaction, and the number of photons that got absorbed by the sample material. The input parameter file to the code is a template where the user fills in the material type, film coordinates, number of histories to track, and some information about the x-ray generator (voltage, current, exposure time, target material and so on).

When a photon falls upon the sample it will either interact with the sample material or it will pass through without interaction. The mean free path (mfp) is the average distance between two interactions points of the photon, this distance is a function of the photon energy, sample material type and thickness. The actual distance traveled by a photon before it interacts with the object material has a distribution function around the mfp value. This distance is determined in the following manner: Let $I(x)$ be the intensity of photons that have not collided after penetrating the distance x into the sample material. Then in traveling an additional distance dx , the intensity of the uncollided flux will be decreased by the number of photons that have interacted with the sample material (either via photoelectric absorption or via Compton scattering) in the thin sheet of sample material having a thickness of dx . The decrease in intensity is easily derived from the attenuation of the beam between x and dx and the resulting removal rate of particles from the beam $I(x)$ as it travels through dx is:

$$-dI(x) = \mu_t I(x) dx \quad (3.9)$$

where μ_t is the total linear attenuation coefficient (due to photoelectric absorption and Compton scattering). The probability that a particle that survived the distance

x , will suffer an interaction in dx is

$$\frac{-dI(x)}{I(x)} = \mu_t dx \quad (3.10)$$

Now let the quantity $p(x)dx$ be the probability that a photon will have its first interaction in dx in the neighborhood of x . This is equal to the probability the photon survives up to x without an interaction *times* the probability that it does interact in the additional distance dx :

$$p(x)dx = e^{-\mu_t x} * \mu_t dx \quad (3.11)$$

integrating equation 3.11 over the distance x :

$$\int p(x)dx = \int_0^x e^{-\mu_t x} \mu_t dx = -e^{-\mu_t x} \Big|_0^x \quad (3.12)$$

$$p(x) = 1 - e^{-\mu_t x} = \text{a random number from 0 to 1,} \quad (3.13)$$

solving for x , the distance the photon will travel before its first interaction:

$$x = \frac{-\ln(1-r)}{\mu_t} = \frac{-\ln(r)}{\mu_t} \quad (3.14)$$

where x is the actual distance traveled by the photon before it interacts with the object material.

If the distance x is greater than the sample thickness, then the photon will go through the sample and either hit or miss the film. However if x is less than the sample thickness, then the photon will interact with sample material. The two types of interaction that are of interest in the energy range of industrial radiography are photoelectric absorption and Compton scattering (pair production is important for energies above 1.022 MeV, but since XRSIM does not simulate such high energies,

we will not simulate this type of interaction). If the interaction is photoelectric absorption then the photon will disappear and we terminate the process and start a new photon. However if the interaction is Compton scattering then we have to sample a new energy and direction for the scattered photon.

The Algorithm The energy of the scattered photon will be randomly sampled (within the two extremes allowed by Compton scattering) and the direction of the scattered photon will be used as the rejection function. The sampling and rejection will continue until the combination of the energy and direction satisfies the Klein-Nishina formula. This is done in the following way:

We first start by sampling the energy of the incident photon from the bremsstrahlung spectrum. Then, we calculate the distance x that the photon will travel before it interacts with the object material. If x is greater than the sample thickness, the photon will exit the sample. If it hits the film, the code will convert its energy into exposure using equation 3.7 and start all over again. However, if x is less than the sample thickness, the photon will interact with the sample material. If the interaction is a photoelectric absorption, the photon will disappear and we start again with a new incident photon. However, if the interaction is a Compton scattering, then the photon will lose some of its energy and it will change its direction. The energy of the scattered photon is given by equation 1.5 and there are two extremes for this equation. The photon might suffer a head on collision and scatter with an angle $\theta = 180^\circ$, or it might completely miss the electron and keeps going straight with a scattering angle $\theta = 0$. For $\cos \theta = 1, -1$, we obtain the maximum and minimum energies of

the scattered photon; E'_{max} , and E'_{min} ,

$$E'_{max} = E_0, \quad (3.15)$$

$$E'_{min} = \frac{E_0}{1 + 2E_0/m}. \quad (3.16)$$

The probability of a Compton scattering at a certain angle θ is given by the Klein-Nishina formula for the differential cross section with respect to the photon energy [19]:

$$\frac{d\Sigma_{Compt}}{d\varepsilon} = \frac{X_0 n \pi r_0^2 m}{E_0} \left(\frac{1}{\varepsilon} + \varepsilon \right) g(\varepsilon) \quad (3.17)$$

where

X_0 = mean free path of photons in the object (cm),

n = electron density (electron/cm³),

r_0 = classical electron radius (cm),

m = electron rest energy (MeV),

E_0 = incident photon energy (MeV),

E' = scattered photon energy,

$\varepsilon = E' / E_0$,

$g(\varepsilon) = \left(1 - \frac{\varepsilon \sin^2 \theta}{1 + \varepsilon^2} \right)$ is called the rejection function, and θ is the scattering angle.

We will sample $f(\varepsilon) = \frac{1}{\varepsilon} + \varepsilon$ over $(\varepsilon_0, 1)$ where $\varepsilon_0 = \frac{1}{1 + 2E_0/m}$, corresponds to the minimum energy of the scattered photon (at a scattering angle of 180°). The rejection function $g(\varepsilon)$, will be used to judge our sampling of the energy and the scattering angle θ . Start by factorising $\left[\frac{1}{\varepsilon} + \varepsilon \right]$ over $(\varepsilon_0, 1)$ as follows

$$f(\varepsilon) = \frac{1}{\varepsilon} + \varepsilon = \sum_{i=1}^2 \alpha_i f_i(\varepsilon) \quad (3.18)$$

where

$$\alpha_1 = \ln(1/\varepsilon_0), f_1(\varepsilon) = \frac{1}{\ln(1/\varepsilon_0)} \left(\frac{1}{\varepsilon}\right), \varepsilon \in (\varepsilon_0, 1) \quad (3.19)$$

$$\alpha_2 = (1 - \varepsilon_0^2)/2, f_2(\varepsilon) = \frac{2\varepsilon}{(1 - \varepsilon_0^2)}, \varepsilon \in (\varepsilon_0, 1) \quad (3.20)$$

We sample f_1 by letting

$$\varepsilon = \varepsilon_0 e^{\alpha_1 \zeta} \quad (3.21)$$

where ζ is a random number drawn uniformly on the interval $(0, 1)$. To compute the rejection function $g(\varepsilon)$ it is necessary to get $\sin^2 \theta$. Let

$$t = \frac{mc^2(1 - \varepsilon)}{E_0 \varepsilon}. \quad (3.22)$$

Then using equation 1.5, we have

$$\cos \theta = \frac{(E_0 + mc^2)E - E_0 mc^2}{E_0 E} = 1 + \frac{mc^2 \varepsilon - mc^2}{E_0 \varepsilon} = 1 - t. \quad (3.23)$$

Thus

$$\sin^2 \theta = 1 - \cos^2 \theta = (1 - \cos \theta)(1 + \cos \theta) = t(2 - t). \quad (3.24)$$

The sampling algorithm was as follows:

1. Compute the parameters that depend on E'_0 , ε_0 , α_1 , and α_2 .
2. Sample ε in the following way: If $\alpha_1 \geq (\alpha_1 + \alpha_2)\zeta_1$ use $\varepsilon = \varepsilon_0 e^{\alpha_1 \zeta_1}$. Else, use $\varepsilon = \varepsilon_0 + (1 - \varepsilon_0)\varepsilon'$ where ε' is determined from:

$$\begin{aligned} \varepsilon' &= \max(\zeta_3, \zeta_4) \quad \text{if } E'_0 \geq (E'_0 + 1)\zeta_2 \\ \varepsilon' &= \zeta_3 \quad \text{otherwise} \end{aligned}$$

3. Calculate t and the rejection function $g(\varepsilon)$. If $\zeta_5 < g(\varepsilon)$, reject and return to step 2.

After selecting the energy and the angle of the scattered photon, the azimuth angle is isotropic and randomly sampled between 0 and 360° . A look up table is then used to find the corresponding photon interaction cross sections and to calculate the new x before the next scattering event. The process is repeated until the photon is either absorbed or exits the object.

Finally, when photons exit the object in the direction of the film, part of their kinetic energy is deposited on the film and its effect on the film is measured by the exposure calculated from equation 3.7. A flag in the code discriminates between the photons that hit the film after scattering and those who went through the object without interaction. The code finally puts out the exposure due to the uncollided flux and the exposure due to the total flux (their ratio is the buildup factor).

Parallel Processing of the Code Monte Carlo techniques are inherently computationally expensive, and for this particular application the method is even more expensive. In this particular situation the incident photon beam has a white spectrum of energies ranging from few keV to the tube voltage. For low energies, the photoelectric absorption is dominant and therefore most of the low energy photons get absorbed and do not contribute to the information necessary to calculate buildup factors. Photons that survive the first scattering event lose some of their energy and as a result their chance of surviving a second scattering event decreases, yet as long as they are not absorbed they carry useful information and we need to keep track of them. This causes further increase in the inefficiency and makes the code even more computationally expensive. Although the code is only used to calculate buildup factors and not to generate radiographic images, its execution time is still impractical

and it increases exponentially with the thickness of the sample.

There are two approaches to multiprocessing a problem: Single Instruction Multiple Data (SIMD), and Multiple Instruction Multiple Data (MIMD). In the SIMD approach each one of the processors is executing the same operation with different data. Direct communication between the processors is not possible except for the nearest neighbor. This approach is most appropriate for matrix multiplication and an example of a machine that uses this approach is the MasPar. MIMD systems have two classes: shared memory and distributed memory. Shared memory architectures are composed of a varying number of processors and they all share the memory. This architecture has the ability to execute different instructions on each of the processors by using different data streams. Examples of systems with this architecture are the CRAY machines (Y-MP and C-90). Distributed memory architectures are composed of a number of processing nodes, each contain its own processor(s), local memory and communications interfaces to other nodes. Such systems are scalable, have no shared memory among the processing nodes, exchange data through their network connections, and execute independent (multiple) instruction streams by using different data streams. The most popular architecture in this class is the hypercube [20].

A network can be thought of as a shared memory architecture where all the nodes share the memory of a master node. The master node distributes the work between the processors on the network and receives the results. A tool that creates such an environment on a network is the C-Linda programming language. This is more like a coordination language between the different processors. C-Linda can be implemented on both shared and distributed memory machines and also on a network of UNIX workstations in which case the environment is called Network Linda [21].

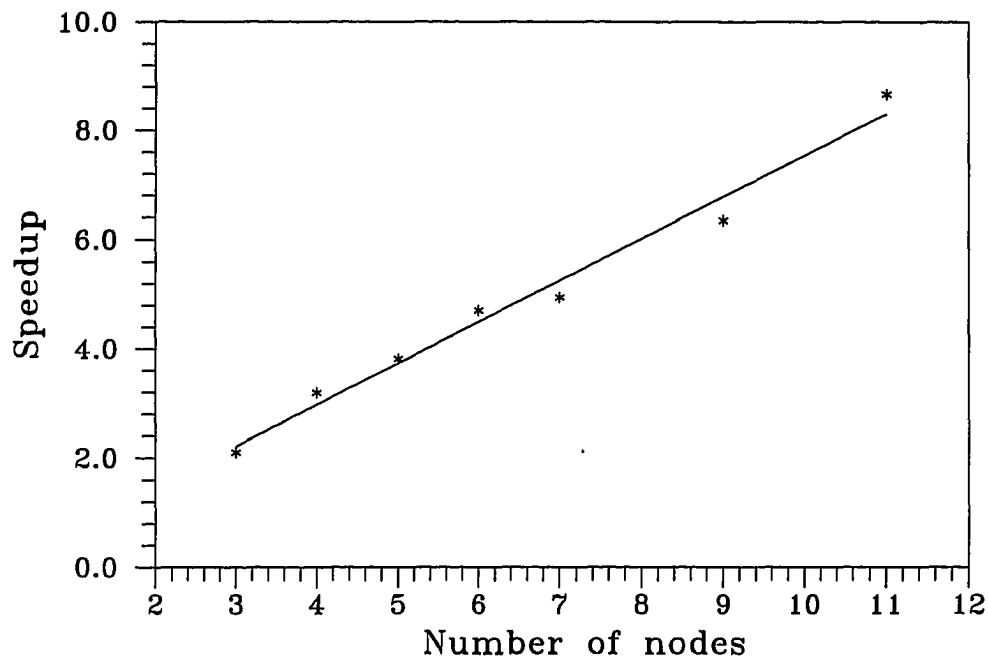


Figure 3.7: C-Linda performance with increasing number of nodes

Network Linda consists of operations that can be added to the driver program to convert the code from sequential to parallel. These operations organize the flow of information between the master node and the processing nodes. Based on the data dependability in the particular problem, some operations have to be blocked until others are finished and so on. The Network Linda specifies the node where the driver program is running as the master node, and its memory as the shared memory (tuple space), and the rest of the nodes are referred to as workers. Only six commands are needed to organize the communication between the tuple spaces and the different processors.

The Network Linda is a scalable environment, the number of workstations that will be accessed as workers is a user input. A list of these workers (nodes) is specified

in a file called "tsnet.nodes". The speedup in the execution time is defined in the following manner; let t_j denote the time of execution for a given job on j parallel processors. The speedup, S_p , for a system of p processors is defined by:

$$S_p = \frac{t_1}{t_p} \quad (3.25)$$

As shown in Figure 3.25, the speedup that can be obtained is a function of the number of nodes used. For certain applications where not much communication between the master node and the workers is needed, the speedup could be linear with the number of nodes. The speedup keeps increasing with the number of processors until it reaches a plateau. This happens when the execution time of the serial portion of the code and the overhead time needed for creating the tuple spaces and for organizing the communication between processors is significant relative to the time spent in executing the parallel portion of the code.

Monte Carlo applications are inherently a good example candidate for parallel processing. On the other hand, for some applications the network traffic can significantly slow down the process and reduce the speedup gain obtained by increasing the number of worker nodes. For optimum utilization of the computation power the network traffic should be kept to a minimum. Theoretically, the more processors are used the more the deviation from a linear speedup. This is due to the increasing overhead time necessary to organize the work between the worker nodes [20].

The parallel code described above has been tested in three independent ways to make sure that it correctly simulates the photon transport through matter. The first test was to balance the total number of photons, where the total number of photons must equal the sum of the three possible events that might take place; absorption by the target, interaction with the film, or losing the photon in a direction away from

Table 3.1: A balanced output of the parallel code

NUMBER OF PHOTONS ABSORBED BY TARGET WAS	4838
NUMBER OF PHOTONS INTERACTED WITH FILM WAS	85154
NUMBER OF PHOTONS MISSED THE FILM WAS	1272
NUMBER LOST IN DIRECTION OPPOSITE FILM WAS	8736
TOTAL	100000

the film. Table 3.1 shows an example of the balanced output from the parallel code.

The second way in which the code was tested was to compare the output of the code to the output obtained experimentally. The energy spectrum that reached an x-ray film placed behind a block of aluminum with a thickness of 0.75 inch was compared to a one obtained experimentally. The result is shown in Figure 3.8, where the two simulated spectrum came to within 20% of the actual spectrum. The last test was to compare the output of the code to an output of one of the other Monte Carlo codes. The one that was available for us is the EGS4 code. Figure 3.9 shows the spectrum that appeared behind a 0.75 inch thick block of aluminum from both codes. Again our simulated spectrum came to within 2% of the EGS4 simulated spectrum.

Results and Conclusions

Experiments were carried out to measure exposure buildup factors for aluminum at several thicknesses when exposed to x-ray white spectrum with a maximum energy of 100 keV. The result is shown in Figure 3.12. As we would expect, buildup factors increase as the thickness of the object increases.

On the same figure shown is the results of the simulation code. All the calculated values lie within 10% of the measured ones. One source of systematic error

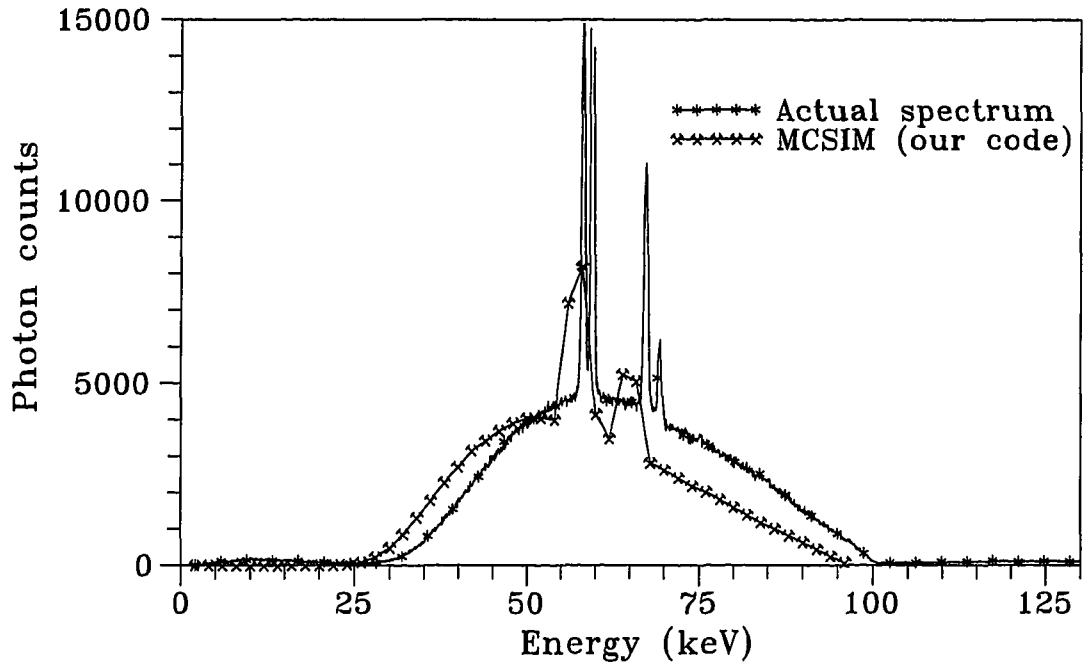


Figure 3.8: Measured and simulated energy spectrums behind a 0.75 inch thick aluminum block at tube voltage of 100 kv

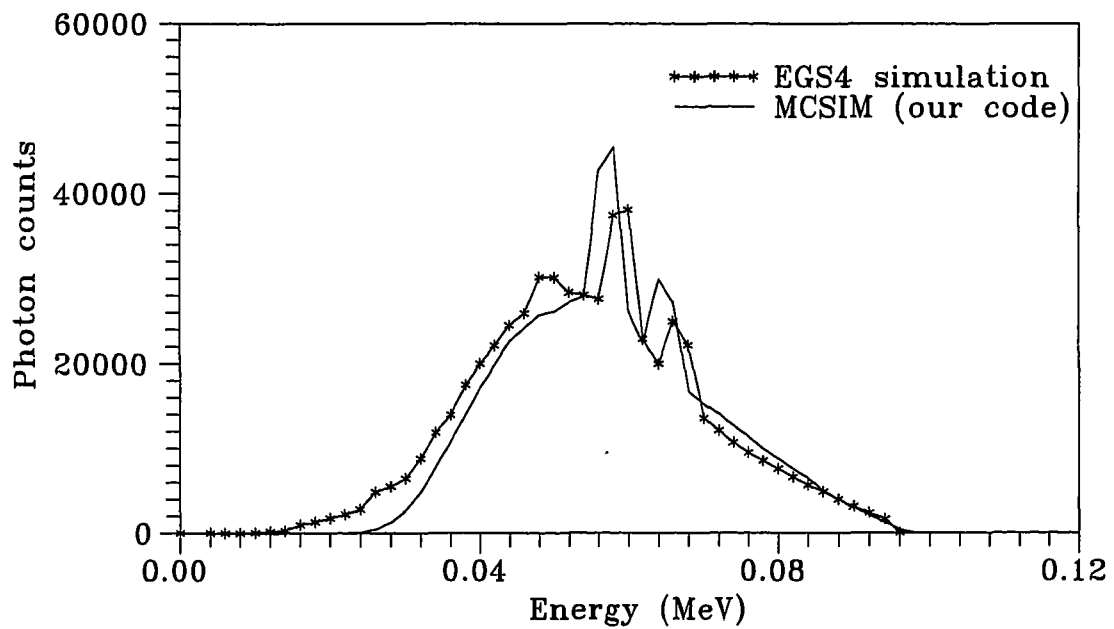


Figure 3.9: Comparison between the outputs of the EGS4 and our code. The energy spectrums behind a 0.75 inch thick aluminum block at tube voltage of 100 kv

in the calculated values is the fact that we had to use the high energy end of the bremsstrahlung spectrum to cut down the execution time. As explained earlier, this is due to the fact that most low energy photons get absorbed and do not contribute to the calculation of buildup factors. As the thickness of the sample increases, more histories need to be tracked before a stable value of the buildup factor can be reached. Using the whole bremsstrahlung spectrum to calculate the buildup factor at 0.25 inches of aluminum did in fact reduce the systematic error by 20% but could not account for all the systematic error in the technique.

Repeating the same experimental procedure to measure buildup factors for steel uncovered an interesting phenomenon which went un-noticed when we did the experiments for aluminum. The contribution of scattering of photons from structures inside the x-ray vault and back into the detector became significant relative to the primary beam that is reaching the detector through the steel block and the collimator. This phenomenon existed when we were working with aluminum, but the relative importance of the scattered radiation compared to the primary beam was low when the material was aluminum. When working with aluminum, attenuation of the main beam was relatively low (compared to steel) and therefore the backscattered radiation from the structural materials and into the detector was insignificant. However when using steel to attenuate the main beam, we found that the scattering from the structures has a relatively high intensity but as would be expected with low energies. This is illustrated in Figures 3.10 and 3.11, where the plot on the top in Figure 3.10 shows the intensity-energy distribution obtained while the generator has no collimation and the steel block was placed in front of the detector. In this configuration the photon beam that goes through the object and into the detector is

heavily attenuated while the scattered radiation from the structure in the vault is not affected. The bottom plot, however, shows the intensity-energy distribution while the steel block is placed right in front of the source. In this configuration both the direct beam that goes into the detector through the collimator and the beam that scatters from the structure are equally attenuated and hence the scattering contribution is insignificant. The same configuration was repeated using aluminum instead of steel and the result is shown in Figure 3.11. The figure indicates that the intensity of scattered photons from the structure is much lower than the intensity of the primary beam that went through the 0.75 inch thick aluminum block, the collimator, and made it to the detector. In fact in the case of aluminum, the areas under the two curves agree with each other to within 9%. It should be noticed that this scattering contribution did not account for the systematic error observed earlier. The scattered photons observed in this phenomenon have low energies and therefore insignificant contribution to the deposited energy on the film.

The execution time to calculate the buildup factor for a 2 inch aluminum block in Figure 3.12 was 25 hours using 10 DEC5000/240 workstations running in parallel. The value at 0.25 inches needed 4 hours.

XRSIM code was modified to access a table of buildup factors and two images were generated to show the difference in film optical density as a result of using buildup factors. The images are shown in Figure 3.13.

An important restriction on the usage of buildup factors is the situation when there is a severe change in the material thickness or type. It should be noticed that buildup factors were defined and measured for smooth and well behaving surfaces and away from the edges. Sharp changes in the material thickness and their effect

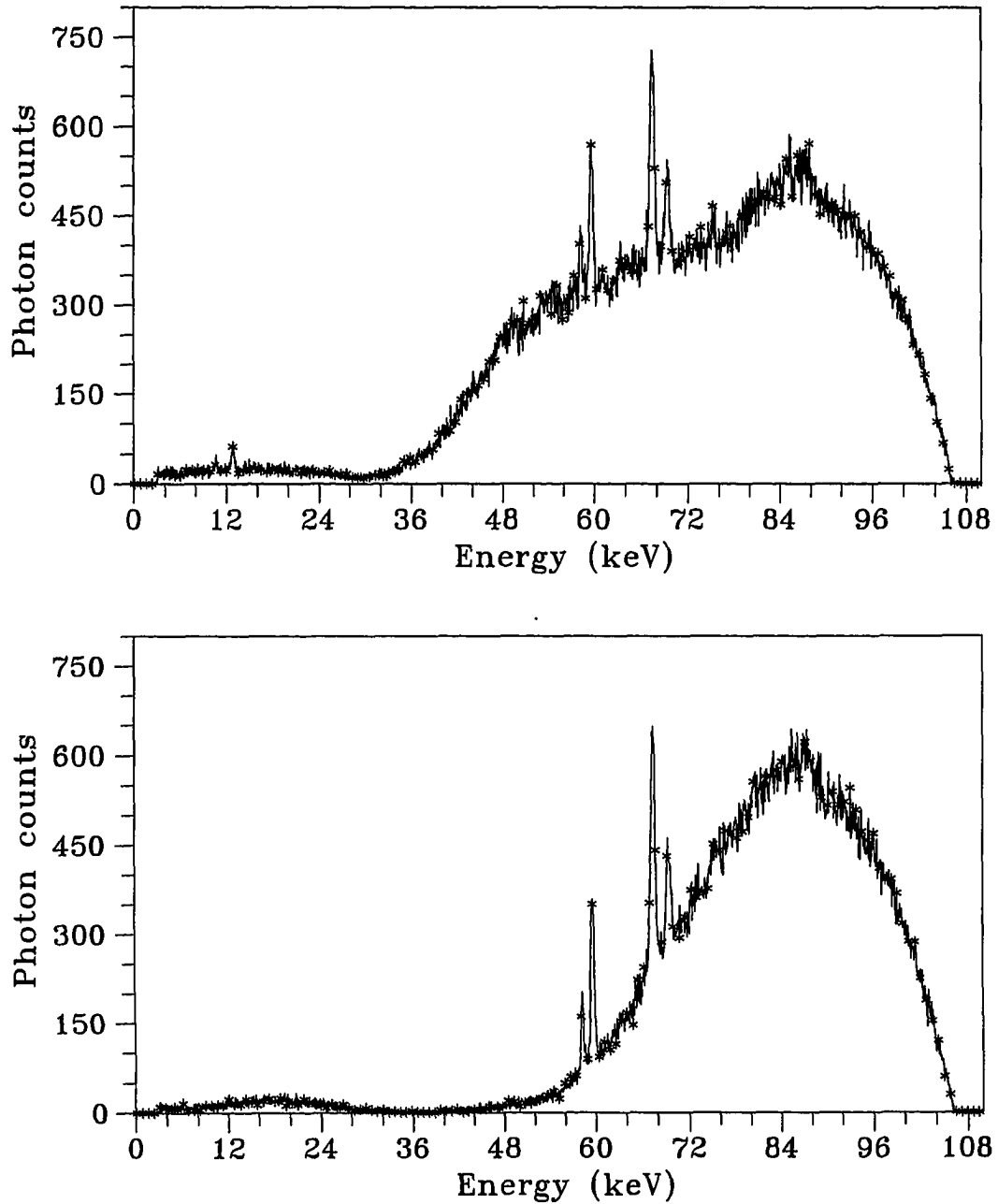


Figure 3.10: Measured primary and scattered fluxes emerging from a rectangular steel block at 106 kV in which the steel block is placed in front of the detector (top) and in front of the source (bottom).

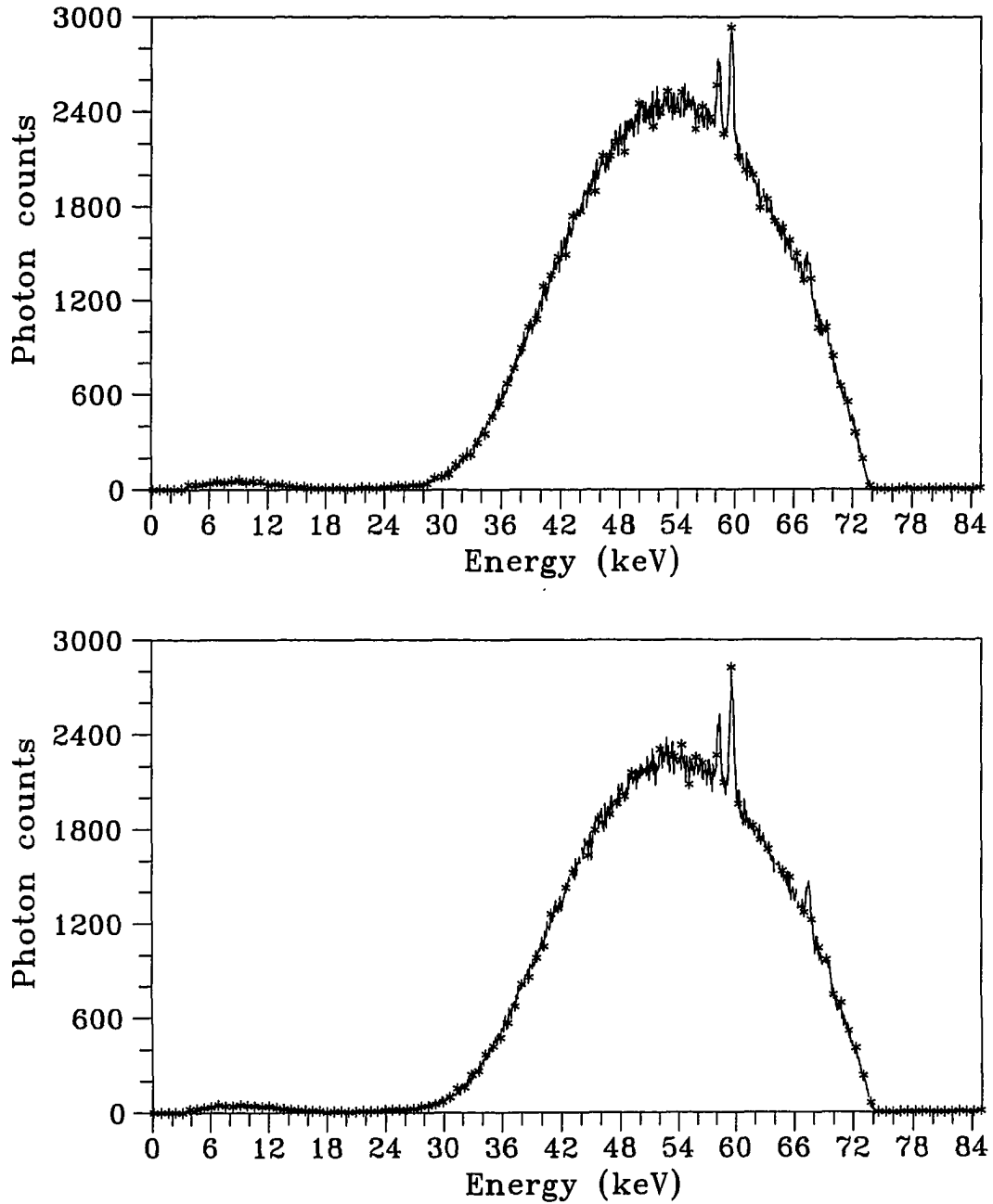


Figure 3.11: Measured primary and scattered fluxes emerging from a rectangular aluminum block at 74 kv in which the block is placed in front of the detector (top) and in front of the source (bottom).

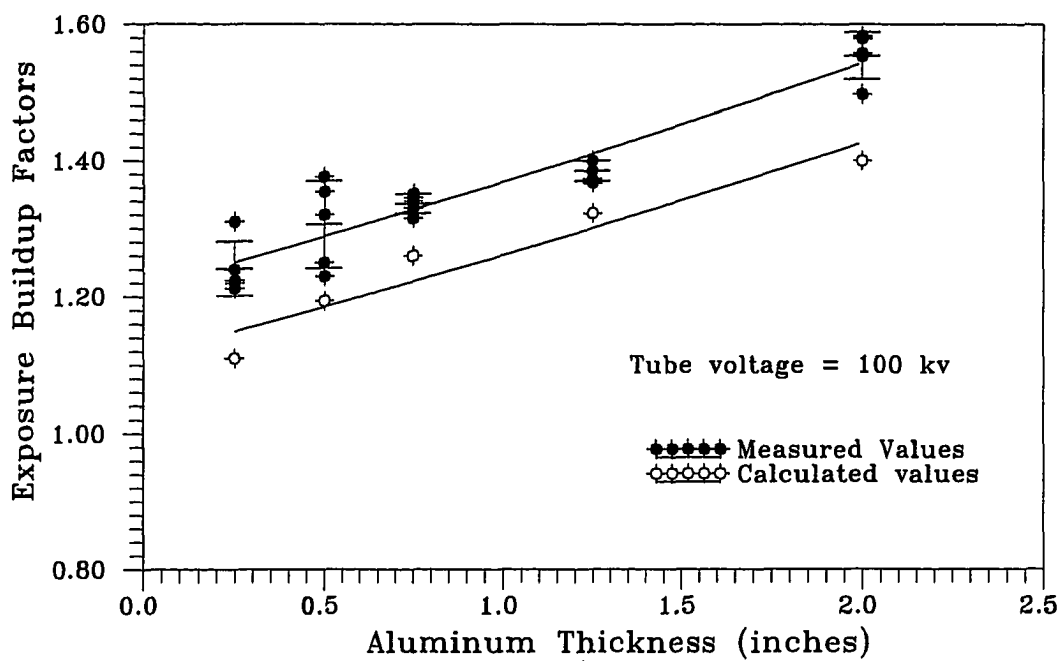


Figure 3.12: Measured and calculated buildup factors for aluminum



Figure 3.13: Experimentally obtained image (left) compared to the output of XR-SIM after integrating the buildup factors to account for scattering (right).

on image quality will be discussed later in this chapter.

Scattering Unsharpness

A radiographic image is more easily visible if its outlines are sharply defined rather than blurred. When a radiograph is taken of a physical sharp edge with an incident beam parallel to the edge, the ideal film response should be a step change in optical density. The size of the step change in the optical density reflects the size of the step change in the sample thickness. In practice, however, the change in the optical density due to a step change in the specimen thickness is continuous as shown in Figure 3.14. This continuous change in the film density is called the “edge or line spread function”.

There are three sources or kinds of unsharpness: geometric, inherent (of the film), and scatter. The geometric unsharpness U_g , is due to the size of the focal spot on the target of the x-ray generator and the thickness and arrangement of the object. The effect of this source of unsharpness can be minimized by arranging the experimental setup such that incident beam is perpendicular to the object and the source to object distance is very large (> 100 cm). The inherent unsharpness U_f of the film is especially important in high-energy x-ray radiography. It is mainly due to the photon scattering in the film plane and will be discussed in more detail in the next chapter. The third source of unsharpness is scattering unsharpness and is due to the fact that more photons are scattered from the thicker part of the object to the thinner side than the other way around. In this section we will consider the contribution of scattering unsharpness to the total unsharpness.

Unfortunately we can not account for scattering across a thickness change by

● Source

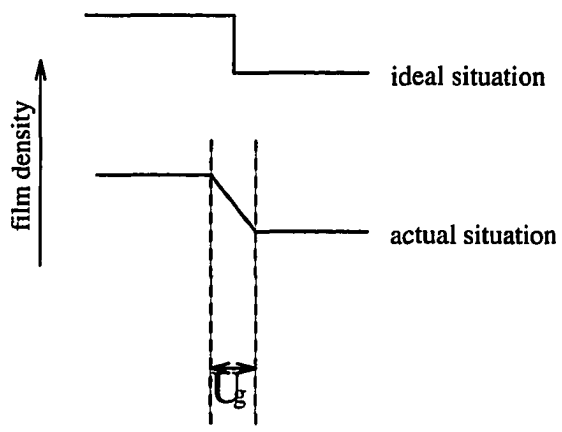
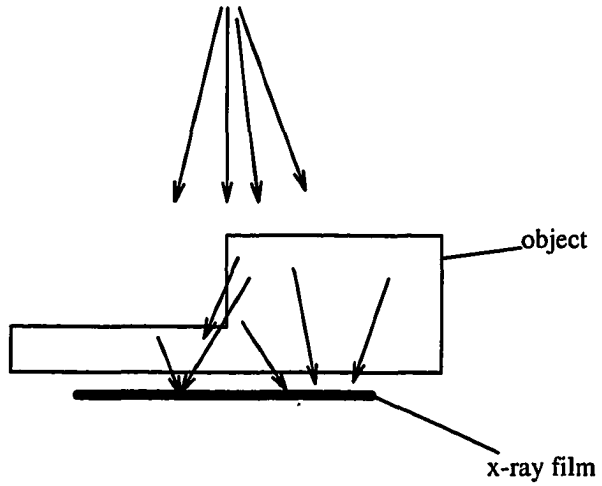


Figure 3.14: Image Unsharpness

using the buildup factors discussed earlier. These factors are limited to smooth and well behaving surfaces only, and hence a different approach has to be followed here.

The contribution of scattering in the object to the image unsharpness can be isolated using a Monte Carlo simulation code. The code can simulate a perfect point source and generate the line spread function across the edge with no scattering in the film plane. It turned out that the shape of the spread function that describes the blur that is due to scattering within the object, depends on the ratio between the fractions of scattered photons from both sides of the edge [22]. The spread function takes three general shapes depending on whether the ratio of the scattered photons from one side of the edge to the other side is less than, equal to, or greater than one. However the relative contribution of scattering within the object to the film unsharpness seems to be negligible for thicknesses commonly used in radiography. Figure 3.15 was generated using a step edge of 4.5 cm of aluminum (the base height was 0.5 cm), with a tube voltage of 100 keV. The effect of scattering from the thick part of the block to the thin part is noticeable when we examine the scattered flux alone. However, as the case in practical applications of radiography, when we look at the total flux across the edge the scattering contribution is not noticeable. Hence the film unsharpness is probably due mainly to the undercut in the film plane itself and the contribution from scattering across the step edge is of less significance.

This conclusion was confirmed by earlier studies done by R. Halmshaw where he stated that the suggestion that "scattered radiation increase image unsharpness, there appears to be very little experimental evidence to confirm such beliefs, and a large number of experiments performed by the author (Halmshaw) have failed to convince him that there is any such effect" [4]. It was also stated by Lawrence E. Bryant and

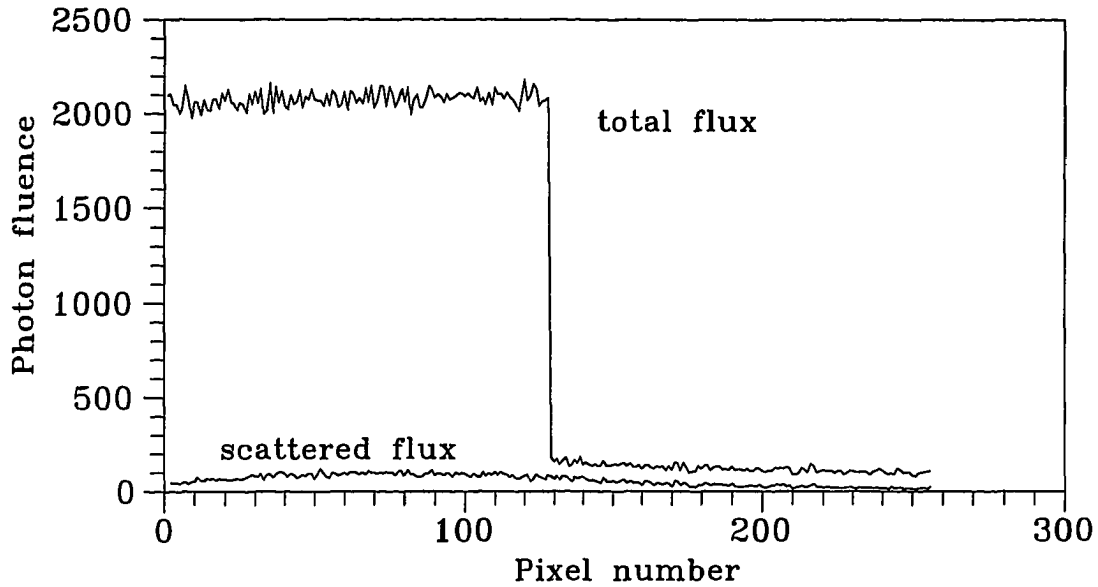


Figure 3.15: Calculated total and scattered fluxes emerging from an aluminum step wedge with a step height of 4.5 cm and a base of 0.5 cm at a tube voltage of 100 kv

Paul McIntire that the geometric unsharpness and the inherent unsharpness of the film are the most important sources of unsharpness. Although the effect of scattered radiation becomes negligible as the thickness difference across the edge decreases, the range of scatter unsharpness might reach few millimeters when the edge thickness is high enough (>10 cm of steel with incident x-ray beam of 31 MeV) [3]. Obviously this is much higher than what we usually encounter in industrial radiography for both the energy and the thicknesses.

CHAPTER 4. FILM UNDERCUT

Introduction

As mentioned in the previous chapter, there are three different causes of image unsharpness (image degradation). These are geometric unsharpness, scatter unsharpness, and film undercut. This chapter will be devoted to develop a model to simulate the contribution of film undercut to the image unsharpness. Simulation of unsharpness is very crucial to accurately simulate the sensitivity limits of x-ray radiography. XRSIM might produce deceiving results that exaggerate the sensitivity limits of the technique because of lack of simulation of the undercut effect (and other sources of unsharpness as well).

A photographic emulsion consists of grains of silver halide, suspended in gelatin and coated onto a support as shown in Figure 4.1. The density and the size of the silver halide grains differs between different types of x-ray films. Fast films usually have large grain size with fewer grains per cm^3 . On the other hand, slow films have high silver/gelatin ratio, involving small grain size and close packing. The difference in the number of silver halide grains per cm^3 is what makes a film fast or slow. Clearly these different types of x-ray films are expected to respond differently to the incident radiation.

When x-ray photons fall upon the film they interact with the silver halide grains.

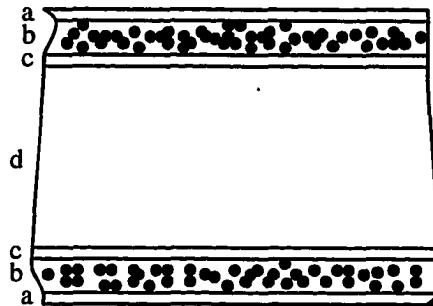


Figure 4.1: Construction of an x-ray film. a:hard gelatin to protect emulsion. b:emulsion. c:substrate to attach emulsion to base, and d:polyester base.

The type of interaction could be photoelectric absorption or Compton scattering. In photoelectric absorption the photon gets absorbed and a photoelectron is emitted, the range of this electron in the film depends on the density of the silver halide and on the energy of the electron. But generally speaking, the range of charged particles in matter is very short and the electron might activate an adjacent grain and settle in a neighboring lattice site. Photons on the other hand, have a relatively very long range in matter. If the photon interaction with the silver halide is a Compton scattering at an angle such that the photon is traveling in the film plane as shown in Figure 4.2, then the scattered photon might activate some of the silver halide grains in its path. The probability of this scenario of course, depends on the photon energy and the material of the scatterer. The higher the energy of the scattered photon, the greater its range will be and the more neighboring grains will be activated.

Measurement of Film Unsharpness

It is possible to isolate the contribution of film unsharpness to the image blurring and to measure it. This is done by making a radiograph of a sharp edge placed close

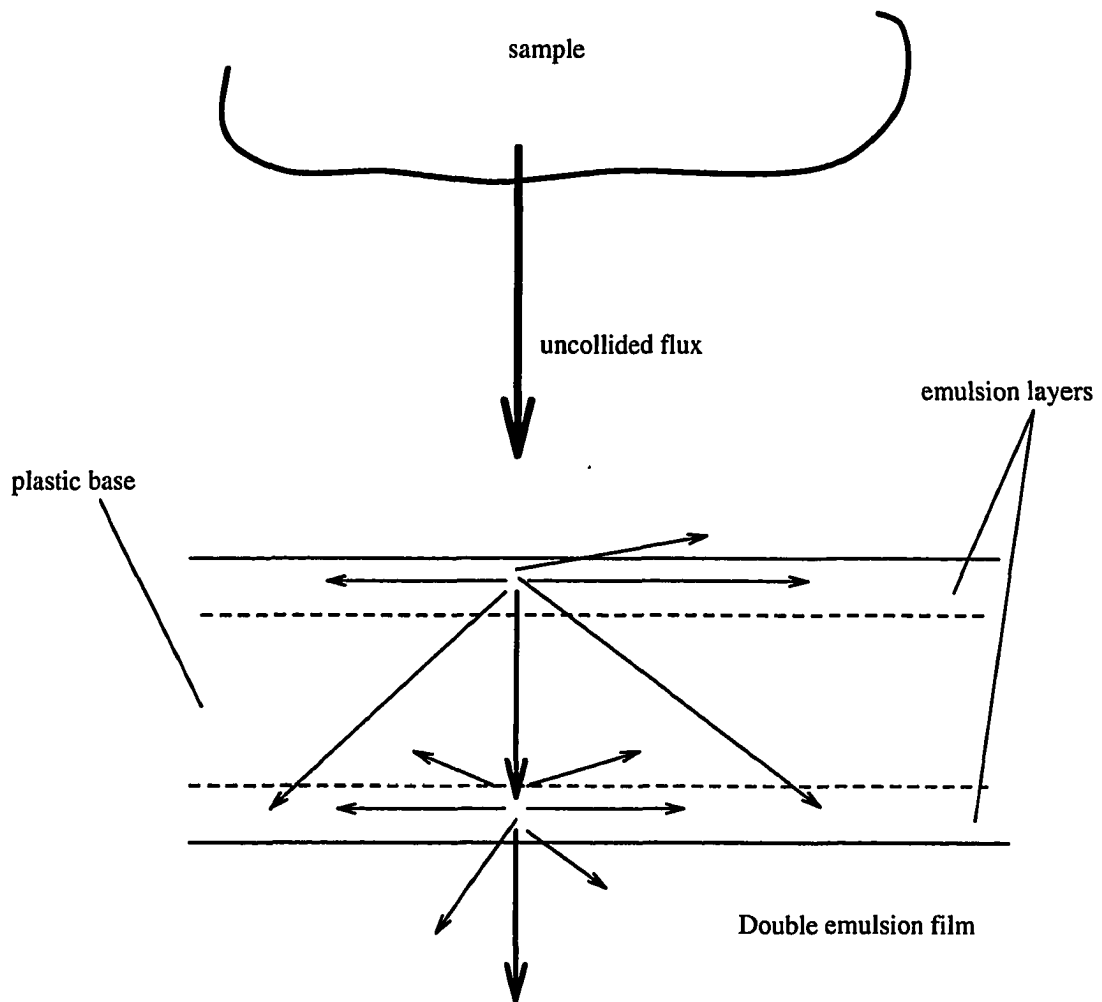


Figure 4.2: Photons might suffer a Compton scattering at an angle such that they travel in the emulsion layer

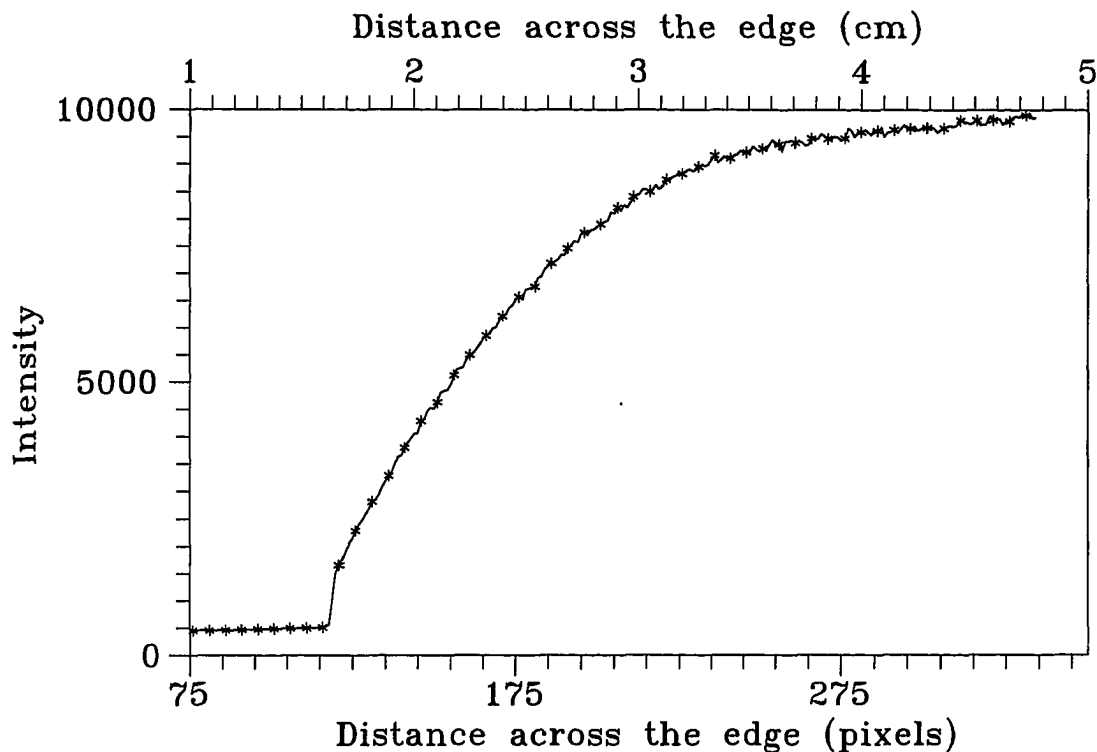


Figure 4.3: Experimental values for film unsharpness obtained for KODAK-AA x-ray film at 100 kV tube voltage

to the film emulsion and accurately aligning the x-ray beam. The source of radiation has to be placed at such a distance that the geometric unsharpness is kept very small. The variation in density on the film across the image of the edge is then measured using a digital scanner. Figure 4.3 shows the undercut after exposing a piece of film using a tube voltage of 100 kV. A lead block covered half of the film and the source-sample distance was 100 cm to insure that the geometric unsharpness is kept to a minimum. The resulting film density was then scanned and scaled on a gray scale using the image processing software "PMIS". The figure shows the part of the film that was covered by the lead block. The film density on the other half of the film

(the uncovered half) was the saturation density of the film. This why the undercut effect in Figure 4.3 is exaggerated, typically an undercut to about half centimeter is encountered in fast films.

It was observed experimentally that the effect of undercut in the film reaches distances of more than half a centimeter at a tube voltage of 100 kV. The mean free path length of a 100 keV electron in aluminum, for example, is $70.3 \mu m$ compared to 2.36 cm mean free path of a 100 keV photon in the same medium, a factor of 335 greater [28]. So, the cause of such undercut must be mainly due to the scattering of photons. However, electrons have a very high damage cross section in matter and therefore the activation of grains next to the edge is mainly due to the recoiling electrons from the Compton scattering.

Simulating the Scattering in the Film Plane

The need to simulate the film undercut arises from the need to improve XRSIM to account for this type of image degradation. The simulation algorithm consists of two major steps; the first is to find the probability of photon scattering at angles such that the beam will travel in the film plane. This probability is governed by the silver halide concentration and the energy of the incident photon and is given by the Klein-Nishina formula. The second step is to find the extent to which the scattered beam will travel before it is attenuated to a negligible intensity. For the second step, we need to know the linear attenuation coefficient of the emulsion layer of the x-ray film. First we measured the density of the silver halide in the film. To get the density of the silver halide we used an electron microscope to generate an image of the x-ray film. We have recorded the photons from the k-fluorescence of the elements in the

Table 4.1: Intensities from the fluorescent for elements in a KODAK-AA film obtained using an electronic microscope at a tube voltage of 30 keV

element	counts/sec.	2σ error
Si	26.6	.0376
Cl	9.07	.1158
K	31.98	.0472
Br	107.84	.0126
Ag	282.58	.0073
Au	27.95	.0582

emulsion layer. The intensities are shown in table 4.1:

The gold that appears in table 4.1 was plated on the surface of the film to improve the electrical conductivity of the film and hence to prevent the accumulation of static charges. The rest of the elements are probably from the gelatin layer that holds the emulsion down (see table 4.1). The table shows that the silver and the bromine are the main constituents of the emulsion layer and hence were taken to be the only significant elements that cause the attenuation of the scattered beam as it travels in the emulsion. A hard copy picture of the surface of the film was taken and the area covered by the silver bromide grain was measured to be 29.6% of the total area. Given that the nominal density of the silver bromide is 6.473 g/cm^3 , then the density of the silver bromide in the film emulsion layer is $0.296 \cdot 6.473 = 1.92 \text{ g/cm}^3$ [29].

To calculate the probability of scattering in the film plane, we start with a bremsstrahlung x-ray spectrum divided into energy bins. Depending on the location of a particular pixel in the film, the incident radiation could be a full spectrum or it could be the bremsstrahlung after being attenuated by the sample material. The film plane is usually divided into pixels of equal areas, each pixel represents a certain

area and a certain direction from the source. A pixel at the edge of the film will most likely see a full bremsstrahlung spectrum, while a pixel that lies underneath the object will see the flux that penetrates the object (a flux with a new energy distribution depending on tube voltage, thickness and material of the object).

For each of the energy bins in the spectrum, we calculate the photon intensity that will interact while passing through the emulsion layer. This is given by the following equation:

$$I(E) = I_u(E)(1 - e^{-\mu(E)x}) \quad (4.1)$$

where $\mu(E)$ is the total linear attenuation coefficient for the silver bromide at energy E , and x is the thickness of the emulsion layer. Depending on the energy of the photon beam and the thickness of the emulsion layer, a fraction of $I(E)$ will interact via Compton scattering. The rest will either be absorbed via photoelectric absorption or will pass through the film without interaction. The fraction that will suffer Compton scattering can be approximated using the following formula, which can be easily derived from the number of photons suffering a Compton scattering divided by the total number of interactions:

$$\frac{\mu_{comp}(E)}{\mu_{total}(E)}, \quad (4.2)$$

where $\mu_{comp}(E)$ is the Compton linear attenuation coefficient, and the denominator is the same attenuation coefficient used in equation 4.1. Now, since we are interested in the portion of the beam that will scatter at an angle of 90 degrees, we can use the Compton scattering formula, equation 1.5 rewritten below, to find the energy of that portion of the beam:

$$E'_\gamma = \frac{E_\gamma}{1 + \left(\frac{E_\gamma}{mc^2}\right)(1 - \cos\theta)}. \quad (4.3)$$

The beam from equation 4.2 will scatter in all directions (4π). To find the part of this beam that will scatter in the film plane ($\theta = 90$ degrees) we use the Klein-Nishina formula, equation 3.17. As mentioned in the previous chapter, the last term in the Klein-Nishina formula is called the rejection function:

$$g(\epsilon) = \left[1 - \frac{\epsilon \sin^2 \theta}{1 + \epsilon^2} \right], \quad (4.4)$$

where ϵ , as defined in chapter 3, the energy of the scattered photon divided by the energy of the incident photon, and θ is the angle of scattering (in this case 90 degrees). If a random number ζ is greater than the rejection function $g(\epsilon)$ then the combination of energy and angle of scattering do not satisfy the Klein-Nishina formula [19]. Therefore the fraction of the Compton scattered beam that will have a scattering angle of 90 degrees is:

$$1 - g(\epsilon) = \frac{\epsilon \sin^2 \theta}{1 + \epsilon^2}. \quad (4.5)$$

The scattering in the azimuth direction is isotropic and one has to correct for the radial divergence in a circle. At this point we have calculated the photon beam that will travel in the film plane (at each energy bin) $I_s(E_s)$. Notice that the subscript s is used to indicate that this is the scattered beam from the energy bin i to the energy E_s . Now, as this scattered beam travels in the emulsion layer, it will interact with the silver bromide, activating that grain. So for each pixel (of the film) in the neighborhood of the pixel where the scattering started, we calculate the flux that reaches it:

$$I_s(E_s) = I_s(E_s) e^{-\mu(E_s)x} \quad (4.6)$$

Notice that the linear attenuation coefficient in the equation 4.6 is at the scattering energy E_s . This scattered photon flux will activate some of the silver halide

grains and its contribution to the final film optical density is obtained from the film model:

$$D_{added} = D_0(1 - e^{-\sigma I(E_s)t}) \quad (4.7)$$

where σ is the film speed. This characteristic of the film measures the efficiency in which a film converts the deposited energy into optical density. This was previously measured for different types of x-ray films as a function of the incident energy. Finally, this density (from equation 4.7) is added to the density generated by the direct beam for each pixel.

Algorithm The simulation step can be summarized in the following algorithm:

1. Starting with the uncollided flux find the portion that will interact within the emulsion layer via Compton scattering using equations 4.1 and 4.2.
2. Use equation 4.5 to find the portion of the beam that will scatter in the film plane where θ is 90.
3. Find the energy of the scattered beam using equation 4.3.
4. Attenuate this beam as it travels in the film plane from one pixel to the next one, using equation 4.6.
5. For each pixel the scattered beam crosses, convert the energy it deposits into added film optical density.
6. Repeat the procedure for all the energy bins and for all the pixels in the film.

Results

A simulation code has been developed to study the effect of undercut on different film types. The results were not surprising, the film undercut is strongly dependent on the film type. Fast films where a small number of relatively large grains are distributed randomly in the emulsion are very sensitive to the undercut effect. Because the grain size is relatively large, activating few of them will produce larger amounts of metallic silver. On the other hand, fine-grain films are not as sensitive because a larger number of grains have to be activated before a significant amount of silver halide is produced. And since the fraction of the photon beam that gets scattered in the film plane is very small, only a few grains get activated and an insignificant amount of metallic silver is produced in fine-grain films as compared to coarse-grain films. The simulation code has confirmed this predicted behavior and Figures 4.4 and 4.5 show the behavior of a coarse-grain film (DEF-5) compared to the behavior of a fine-grain film (KODAK-AA) under different tube voltages and exposures.

Figure 4.4 shows that the effect of undercut on DEF-5 films is significant and the extent of undercut can reach up to 0.5 cm. The effect of undercut, however, drops exponentially as you move away from the point where the original scattering took place, this is because of the attenuation of photons in the silver halide. Reducing the exposure by 50% still produced a significant effect of undercut in the DEF5 films while the effect on the KODAK-AA films is negligible in both cases. Similarly Figure 4.5 shows that reducing the tube voltage from 320 kV to 120 kV reduced the effect of undercut in DEF5 films while KODAK-AA films are not very sensitive to changes in either the exposure (Figure 4.4) or the applied voltage (Figure 4.5).

The algorithm that simulates the undercut effect was integrated into XRSIM and

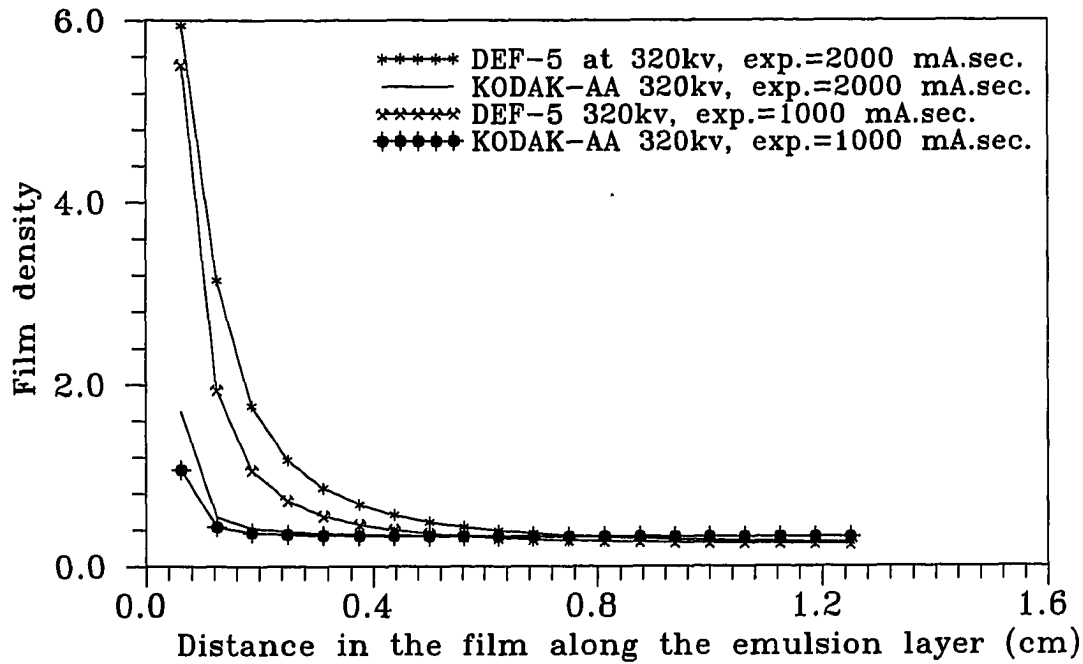


Figure 4.4: Calculated undercut for two different types of x-ray films using the same tube voltage with different exposures

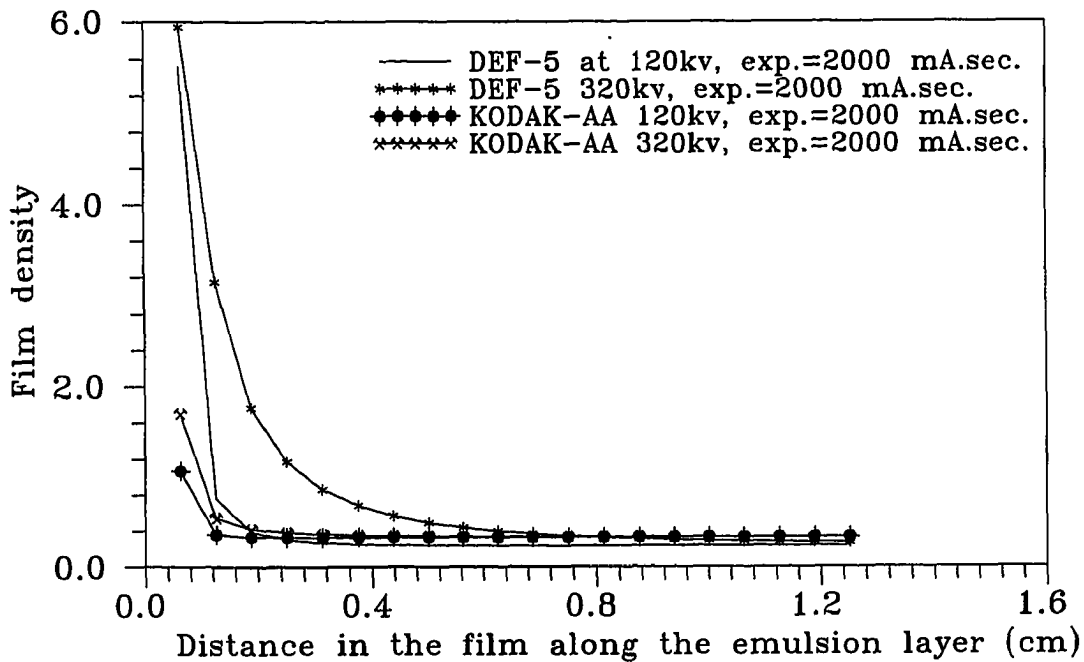


Figure 4.5: Calculated undercut for two different types of x-ray films using the same exposure and varying the tube voltage

an image was generated to demonstrate this phenomenon. Two images are shown in Figure 4.6 to show the effect of undercut. The image to the left was generated experimentally, while the one to the right is a simulated image generated using XRSIM with the film undercut effect simulation integrated into the code. Clearly the undercut simulation is not accurate and a closer investigation of the phenomenon is needed. A simple calculation excludes the possibility that scattering from the first emulsion layer to the second emulsion layer can be of any significance. Even at high scattering angles like for example 60 degrees from the first emulsion layer, the range of the scattered radiation in the second emulsion layer will be 0.31 mm (the plastic base thickness was measured to be 0.18 mm). This leaves two possible sources of error in the undercut simulation algorithm that we did not account for. The first is the fluorescent x-rays emitted due to photoelectric interactions of photons with the silver atoms. The second might be inaccuracies in measuring the silver halide densities when we used the electron microscope.

Integrating the undercut simulation into XRSIM significantly increased the execution time (from less than two minutes to several hours). This called for more optimization of the code to make it more computationally efficient. A way to make the code computationally efficient is to find which part of the bremsstrahlung spectrum generates most of the undercut effect. Then, instead of integrating over the whole spectrum to generate the undercut effect, we integrate over the most significant part of the spectrum. Figure 4.7 compares the undercut contributions from the lower half and the top half of the spectrum to the total undercut due to the whole spectrum. The figure shows that the contribution from the lower half is more significant than the upper half, this is probably due to the higher photon intensity

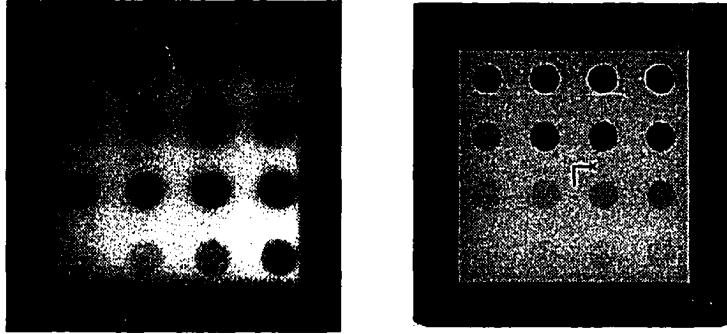


Figure 4.6: Comparison between an image for the Al block generated experimentally (left) and simulated with the undercut effect integrated into XRSIM (right), using DEF-5 films

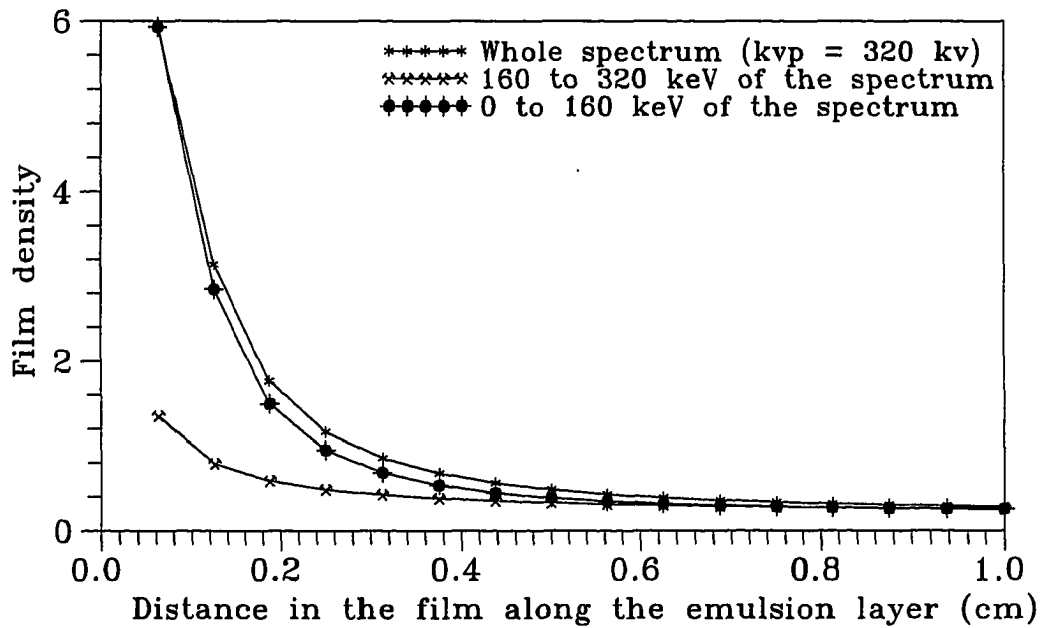


Figure 4.7: Calculated undercut for the upper and lower halves of the spectrum compared to the total spectrum, DEF-5 films, kvp = 320 kv.

at lower energies than in the upper half of the spectrum.

In the low energy half of the spectrum, the first quarter of the spectrum has a more significant effect in the neighborhood of the pixel where the photon scattering took place. This is again due to the high photon intensity in this energy range. However the range of these scattered photons at such low energies is very short compared to the second quarter of the spectrum. This behavior is shown in Figure 4.8.

A more dramatic decrease in the execution time of the code can be achieved if we can find an equivalent energy instead of the energy distribution of the spectrum. This will probably improve the execution time by a factor equal to the number of energy bins that are usually used. Figure 4.9 shows the results of several attempts to find such a value. The closest approximation to the undercut that is due to the whole spectrum is obtained by taking an average value of the energy in the spectrum. This average energy is defined as:

$$E_{av.} = \frac{\sum_i E_i I_i}{\sum_i I_i} \quad (4.8)$$

where E_i and I_i are the energy and the photon intensity of the energy bin i , and the summation is carried over all the energy bins.

Other ways of making the code computationally efficient include performing some of the calculations off line and integrating the results as a lookup table which the code can access and read, instead of doing the calculations on line. Reducing the number of pixels (the distance to which we calculate the undercut) where the undercut is considered to be significant might reduce the execution time. This might significantly reduce the execution time but will underestimate the range to which the undercut effect is accurately simulated.

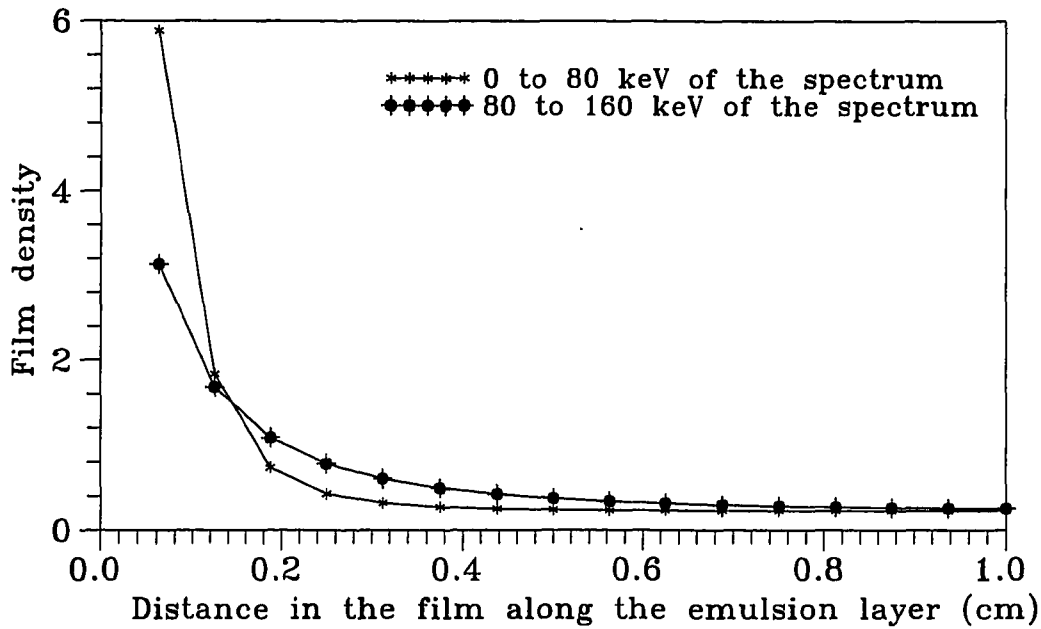


Figure 4.8: Calculated undercut for the first and second quarters of the lower half of the spectrum, DEF-5 films, kvp = 320 kv.

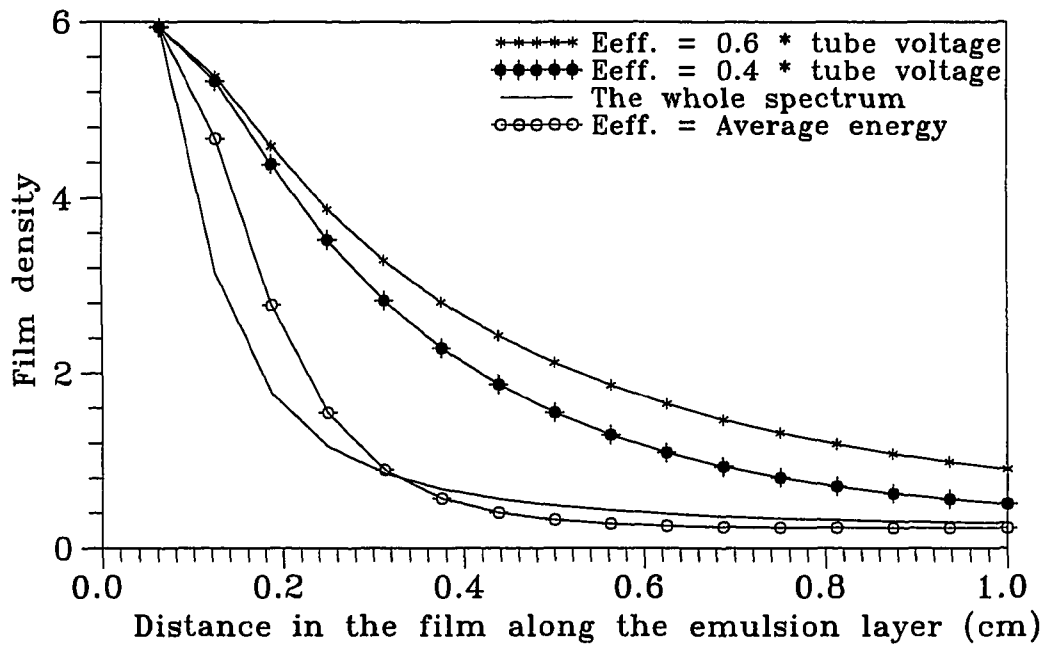


Figure 4.9: Calculated undercut for equivalent energy values and the whole spectrum, DEF-5 films, kvp = 320 kv.

The above calculation, although it simulates the contribution of the photon scattering to the undercut phenomenon, does not account for the contribution of the recoiling electron. The combined effect of both the photon and the electron will result in a significant blurring effect right next to the original pixel because of the high damage cross section of the electron. The extent to which the effect of the electron is significant depends on the energy of the recoiling electron but as explained earlier this range is less than a millimeter.

Although the undercut simulation algorithm gives reasonable results that describe the behavior of the different types of x-ray films under different exposure conditions, an accurate quantitative description of the phenomenon is not possible at this stage. This is due to the lack of accuracy in the film models that the simulation code has employed. These film models have been developed several years ago and recently were found to contain inaccurate data. A new approach to generate new film models based on the results of chapter 3 of this dissertation is being considered. This will allow a more quantitative assessment of both the undercut and the point spread function in the future.

According to R. Halmshaw; film unsharpness is due to electrons recoiling from Compton scattering and activating a neighboring silver halide grain. This happens when "high-energy X-ray quanta having energies greater than is required for ionization the excess energy appears as kinetic energy of the electron. This, therefore, may be ejected into the surrounding emulsion with considerable velocity and may reach an adjacent silver halide grain while still having sufficient energy, on being absorbed, to render this second grain developable" [4], (page 177). We believe that the above argument is inaccurate because of the very short range of charged particles in matter.

In fact, electrons with energy of 100 keV have a very short "mean path length" in matter, on the order of few tenths of a millimeter even in very low density mediums like air [28]. This and the fact that film undercut can be seen in the laboratory to reach ranges up to half a centimeter, led us to believe that the main cause for film undercut must be the scattered photon rather than the electron. Although photons have a relatively low damage cross section compared to charged particles, they can penetrate enough material to account for the ranges seen in the laboratory.

CHAPTER 5. BACK SCATTERING SIMULATION

Introduction

As mentioned earlier, Compton scattering is an interaction of photons with atomic electrons, in which both the energy and the momentum are conserved. The photon interacts with a constant interaction cross section per electron $e\sigma_C$ for all materials at a certain photon energy. However, the Compton scattering cross section per atom, σ_C , is equal to the number of electrons in the atom multiplied by the $e\sigma_C$ [18]:

$$\sigma_C(E) = Z e \sigma_C(E) \quad (5.1)$$

This characteristic means that the higher the atomic number of an element, the stronger the signal obtained from Compton scattering. This is useful for inspecting heavy elements because of the high attenuation coefficients of these elements and the limits they put on inspections with transmission techniques.

Situations where inspection with back scattering is helpful arise when the inspected object is very large, or when access is limited to only one side of the specimen. In these cases photons traveling in the forward direction can not be detected. These situations are fairly common when inspecting airplane wings or when inspecting machine parts without taking them off line. Inspection with x-ray back scattering technique can be performed by detecting photons that have suffered a Compton scat-

tering at large angles, more than 90 degrees. The problem with detecting photons at such large scattering angles is that the cross section for Compton scattering is very low, and consequently the signal from these inspections is weak. However several parameters can be optimized to enhance the probability of a back scattering event. These parameters include the angles of incident and scattered beams, the exposure time, current, and x-ray tube voltage. The orientation of the inspected object should also be optimized to minimize the distance through which photons are attenuated before reaching the detector. Optimizing these parameters for a certain inspection can be made fast, inexpensive and more convenient by using a simulation code.

Several companies have built devices that implement this technique. Boeing has built a device that uses a white spectrum of x-rays with open collimation on the detector side [30]. GA Technologies Inc. has also built a device that uses a mono energetic photon source (Co-60) with collimation on both the source and the detector [31]. However, these devices are still in the experimental stages and have limited flexibility in terms of changing the configurations of the experimental setup. One major application of this technique is the development of a "Backscatter X-ray Explosives Detector" [32]. A soft x-ray beam bounces backward when hitting a light material like plastic explosives. A device that employs this physical phenomena was developed by "American Science and Engineering, Inc." and tested on Heathrow airport baggage. The device was capable of screening bags as they move along an airport conveyor belt at 100 ft. per min. [33]. These systems sell for \$135,000 each, which is much less than the cost of a competing device that uses thermal neutron activation systems. The thermal neutron activation device (TNA) bombards luggage with low energy neutrons and when these neutrons are absorbed by the nitrogen in

explosives, the nitrogen nuclei emit characteristic gamma rays. TNA is also marketed by American Science and Engineering, Inc. and it sells for \$750,000.

This chapter presents a computer simulation of inspection with backscattered radiation technique and describes the effect of different parameters on the inspection outcome. This work is a first step towards the development of a more complete simulation code where more than only one experimental configuration is considered. The back scattering simulation code borrowed two important characteristics from XRSIM that made the code general and flexible to simulate different experimental configurations. These two characteristics are:

1. Interacting with the CAD interface to extract the geometry information of the part: the code reads the output of the CAD software package "IDEAS" and transforms the triangular facet description of the object surface into distances. This gives the code the ability to handle multiple objects with complex geometry, for example, welds and complex structures.
2. Simulation of the x-ray source: The code simulates the interactions of electrons with the x-ray generator target material and calculates a bremsstrahlung spectrum from the basic physical principles. This feature enables the code to simulate different x-ray generator settings as long as the tube voltage is below the cutoff energy of pair production.

User Interface

The user interface with the code is an input data file that includes the user input parameters. These parameters are:

1. The x-ray generator specifications: These are the generator settings, namely, the tube voltage, current and exposure time, x-ray generator target material and angle, and the x-ray generator filter material and thickness. These specifications are necessary to generate the bremsstrahlung spectrum.
2. The name of the CAD file that contains the triangular facets describing the geometry of the inspected object(s).
3. The material type for each of the inspected objects.
4. The option of adding an elliptical flaw and its material.
5. Source and detector collimations.
6. Source and detector locations.
7. Source direction ϕ and angle of back scattering θ .
8. Choice of scanning in the x, y, or z directions.

Figure 5.1 shows the experimental setup that is being simulated at this stage of the code development. The virtual source in Figure 5.1 is the volume of intersection of the two collimators. This volume of intersection appears to the detector as a source of radiation. Of course the size of this virtual source depends on how tight the collimation is on both the source and the detector. As will be explained in the next section, the size of the virtual source will affect the intensity of the back scattered beam.

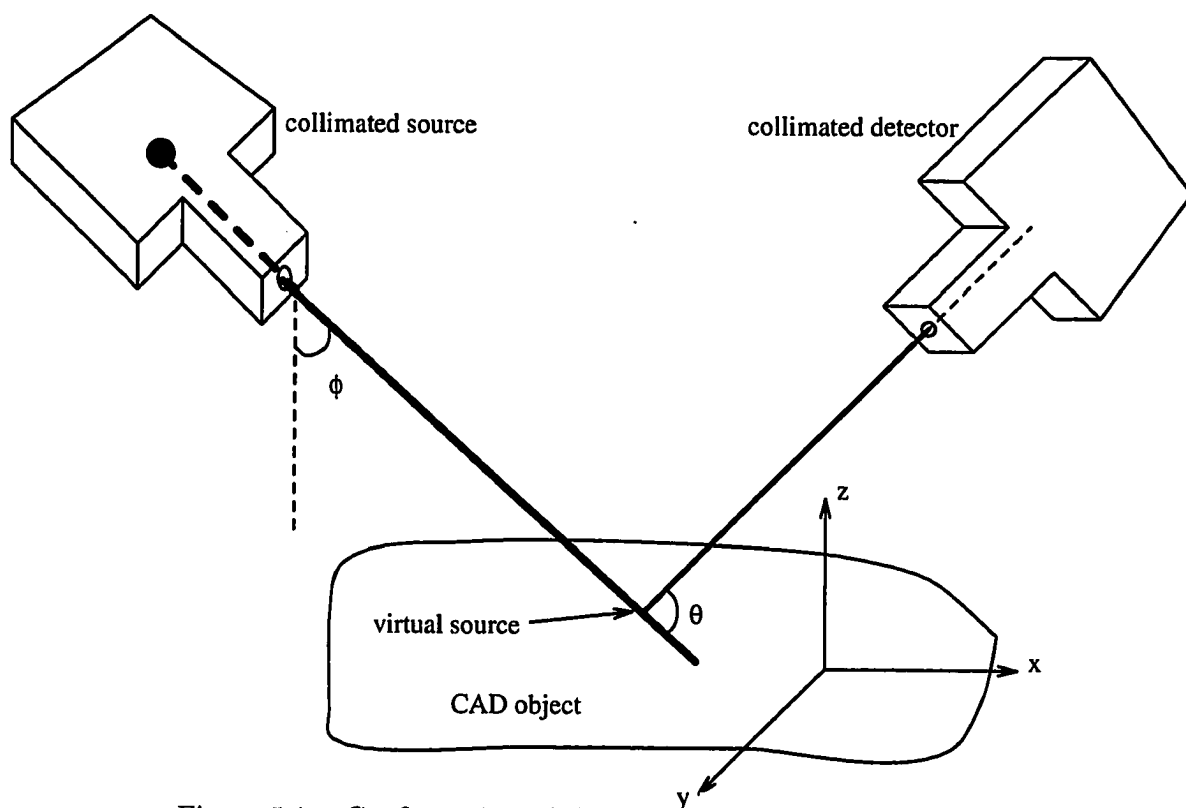


Figure 5.1: Configuration of the simulated inspection setup.

Algorithm

The algorithm for this simulation code is almost identical to the one used for the undercut simulation. As in the undercut simulation, we start with a bremsstrahlung spectrum divided into energy bins. For each energy bin, the intensity of the photon flux after penetrating an initial distance x in the object is given by equation 4.1, where $\mu(E)$ is the total linear attenuation coefficient at a certain energy bin. The intensity of the photon beam that will interact while passing through the virtual source is given by:

$$I(E_i) = I(E_i)(1 - e^{-\mu(E_i)dx}) \quad (5.2)$$

where dx is the virtual source thickness as explained earlier and shown in Figure 5.1. The virtual source volume (and hence dx) is defined by the detector and source collimators. Again we find the fraction that will interact via Compton scattering and will back scatter at an angle of θ . This is done using equations 4.2 and 4.5 except in this case θ is specified by the user instead of being always 90 degrees as in the case of undercut simulation. The resulting photon beam is then attenuated through the material back to the detector using equation 4.6. Again the attenuation coefficients are those at the energy of the scattered photons obtained from equation 4.3. The scattering in the azimuth direction is isotropic and the actual portion of the back scattered beam that will reach the detector is reduced by a certain factor. This factor is obtained from simple geometry and is equal to the ratio of the detector collimator diameter to the circumference of the base of the vertical cone that has its vertex at the virtual source and the circumference of its base includes the collimator diameter.

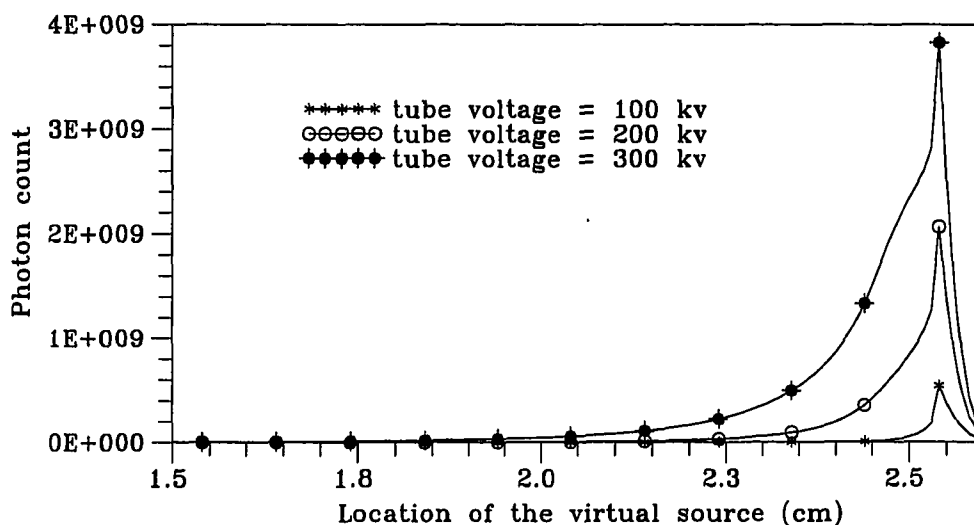


Figure 5.2: Penetration depth in steel at different tube voltages.

Results

Simulations for different inspection configurations have been generated. The base material in these inspections is aluminum with inclusions of different sizes made of different materials. Some examples demonstrating the capabilities of the code include depth profiles, effect of defect type (flaw or inclusion) and effect of flaw or inclusion locations on the back scattered signal, sensitivity to defect size, effect of different back scattering angles, and multiple material inspection.

In situations where inspection is needed at greater depths in the specimen, the tube voltage must be increased. Another situation where higher tube voltages are needed is when the inspected object is made of heavy metal like steel. Figure 5.2 shows that the penetration depth of the beam increases with increasing tube voltage.

The type of the defect, whether it is a void flaw or an inclusion, determines

the shape of the signal resulting from a back scattering inspection. Signals from inspecting a sample that has a void flaw are different from those resulting from inspecting the same sample with an inclusion made of a material heavier than the host material. As the virtual source approaches the host material, the back scattered beam intensity increases until it reaches a maximum when the virtual source is completely inside the host material right by the surface. As the virtual source starts moving in the negative z direction into the object, the back scattered beam intensity is attenuated exponentially. When the virtual source enters the void flaw, the back scattered intensity drops to zero since scattering from a void (assuming the void flaw is full of gas) is negligible. As the virtual source leaves the flaw, the intensity of back scattering increases again.

Figure 5.3 shows the results of three simulated scans, with a void flaw, a Ti inclusion, and a “no flaw” case. When the elliptical flaw (3x2x2 mm) is an inclusion made of a material of a higher density than the host material, the back scattering intensity increases as the virtual source enters the inclusion (instead of dropping to zero in the case of a void flaw). Once the virtual source is inside the inclusion, the direct and the back scattered photon beams will be attenuated through the inclusion material (Ti for example), and that is why the signal drops at a higher rate than for the host object. As the virtual source leaves the inclusion, the intensity starts increasing gradually since the attenuation distance of the back scattered beam in the Ti decreases.

The location of the flaw or inclusion also affects the shape of the resulting signal. Figure 5.3 shows the effect of the defect type on the resulting signal when the defect is in the way of the incident beam. For the same defect type, however, the simulation

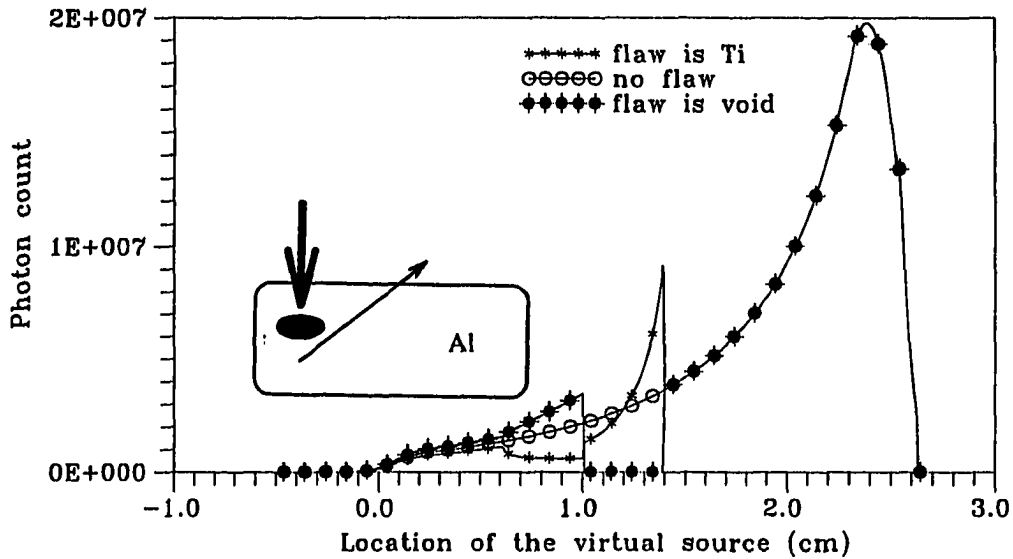


Figure 5.3: The type of defect determines the shape of the resulting signal.

code predicts different signals for the case when the defect is in the way of the incident beam as oppose to the case when the defect is in the way of the back scattered beam as shown in Figure 5.4. When the defect is a void flaw in the way of the back scattered beam, the photon intensity of the back scattered beam increases slightly compared to the "no flaw" case. This is due to the fact that less attenuation of the back scattered beam occurs when it passes through the flaw. On the other hand, when an inclusion made of Ti is in the way of the back scattered beam, more attenuation takes place and the photon intensity drops.

The sensitivity of this technique to different flaw sizes is determined by the size of the collimation on the source and by the step size while scanning in a certain direction. In the case when a void flaw is in the way of the incident beam, the width of the drop in intensity is equal to the flaw size. For the time being, the code does

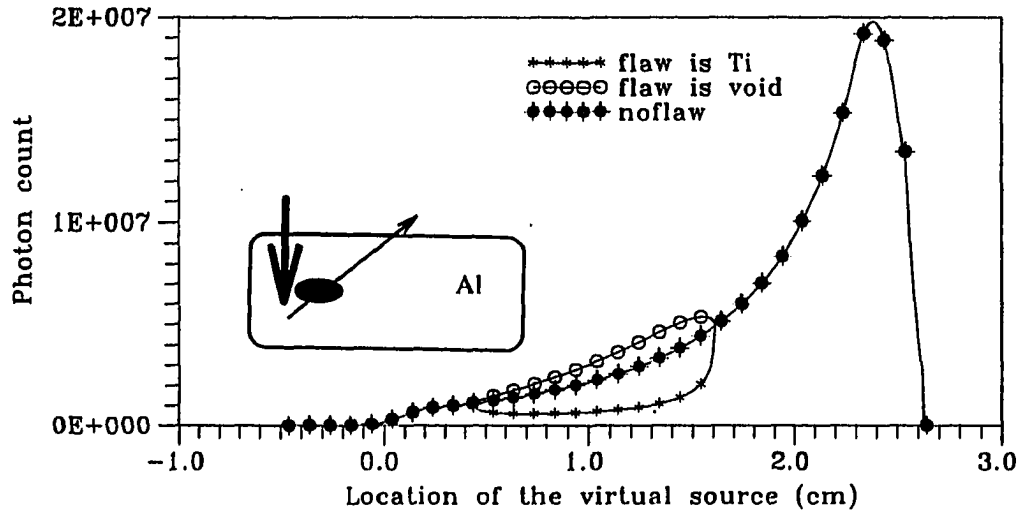


Figure 5.4: Z-scan with the defect in the way of the back scattered beam.

not simulate the gradual approach of the virtual source to the flaw and hence the edge of the drop is a sudden drop rather than a gradual decrease (increase in case of a Ti inclusion) in the back scattered intensity. Once this feature is added to the code, we would expect the edge to be blurred and the simulation would be more realistic. Figure 5.5 shows that the width of the drop decreases as the size of the flaw decreases. Similarly; in the case of an inclusion, the width of the spike is a measure of the inclusion size as shown in Figure 5.6.

Sensitivity to the void flaw or inclusion sizes when the defect is in the way of the back scattered beam has completely different features. When the defect is a void flaw, the intensity increases gradually, since there is less material to go through, until it reaches a peak when the back scattered beam passes through the center of the void flaw. Then it starts to decrease again until the beam is no longer going through the void where the signal coincides with the "no flaw" case. The area underneath the

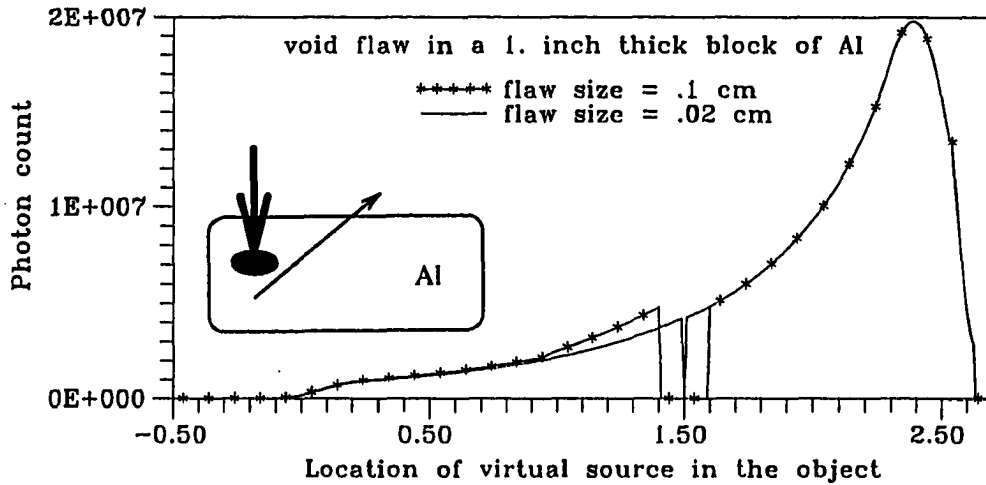


Figure 5.5: Sensitivity towards different flaw sizes when the flaw is in the way of the incident beam.

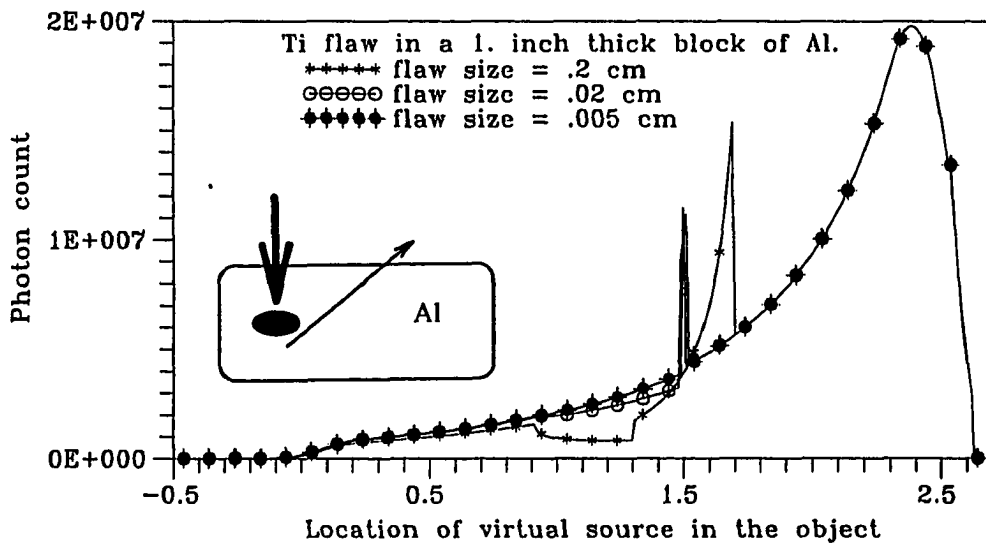


Figure 5.6: Sensitivity towards different Ti inclusion sizes when the defect is in the way of the incident beam.

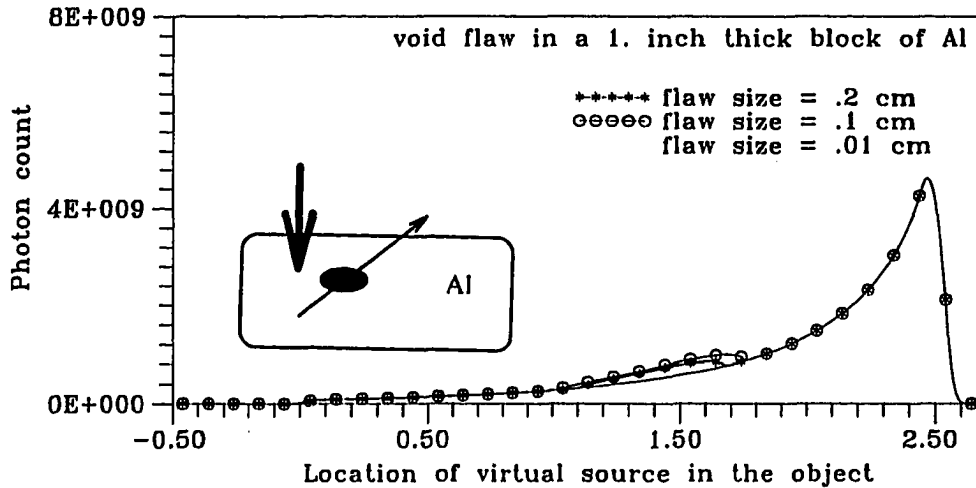


Figure 5.7: Flaw is in the way of the back scattered beam.

hump is a function of the flaw size. As the flaw size decreases, the increase in the intensity decreases to the point where the increase in intensity is within the statistical variation in the x-ray beam. At this point it is no longer possible to distinguish between the variation in the photon counts that is due to a difference in the material thickness and the statistical variation that is inherent in the photon beam. Figure 5.7 shows the signals obtained for several flaw sizes in the way of the back scattered beam. By a similar argument, a drop in the photon intensity is expected when the defect is an inclusion in the way of the back scattered beam and made of a material of a higher density than the host material. The amount of this drop will of course depend on the size and type of the inclusion.

The choice of the source and detector positions and their collimators define the desired scattering angle. The Klein-Nishina formula, equation 3.17, shows that

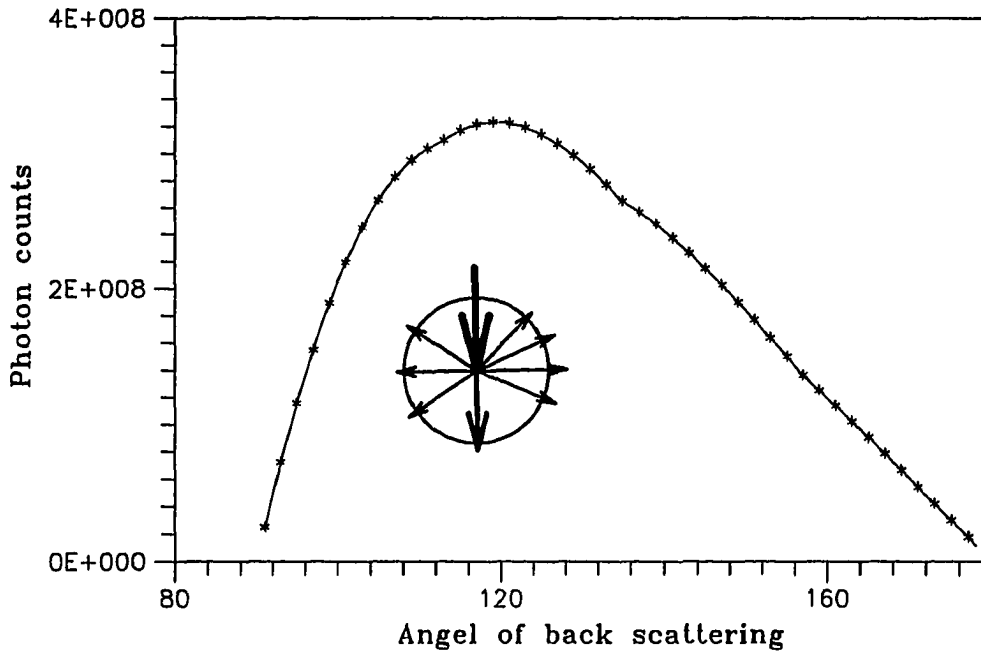


Figure 5.8: Optimizing the scattering angle to maximize the back scattered amplitude.

Compton scattering cross section for a certain material is a function of both the energy of the incident photon and the scattering angle θ . For a certain energy, the intensity of the back scattered beam differs from one angle to the other. Figure 5.8 shows the photon count at different scattering angles when the virtual source is at the center of a 2 cm radius sphere made of aluminum and the incident radiation has a maximum energy of 320 keV. The figure shows that the optimum angle to direct the detector at is 120 degrees.

Finally the code has the ability to simulate the inspection of multiple objects each of which is made of a different material. Figure 5.9 shows the signal resulting from the inspection of two blocks on top of each other. The spike represents the transition from aluminum to titanium and the valley represents a void flaw. Since

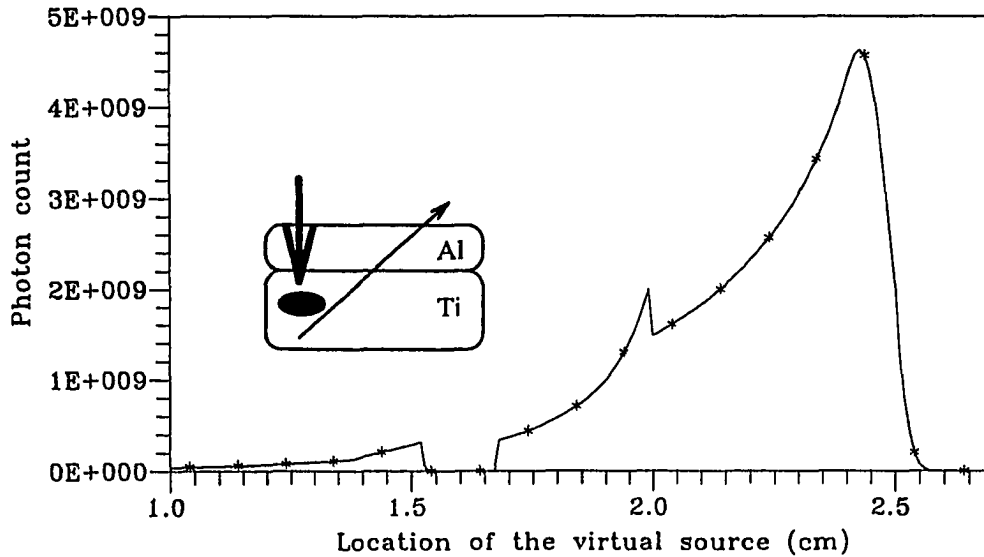


Figure 5.9: Z-scan through multiple materials.

the code interacts with a CAD interface, there is no limit on the complexity of the inspected object. This feature is useful when simulating the inspection of complex structures, assemblies and welds spots.

Conclusion and Future Work

The inspection with Compton back scattering simulation code can be a valuable tool to understand and evaluate the signals resulting from inspections with back scattered radiations. These signals might differ in shape depending on the type of defect, location with respect to both the incident beam and the back scattered beam. Understanding the resulting signals and optimizing the experimental setup to obtain a clear description of the flaw type, size and location can be made easier using this code. The simulation code can be used to train users of this technique to understand the effect of different experimental configurations on the resulting signal

and to interpret the outcome of the inspection. The code is also flexible and it draws its flexibility from the following features:

1. The code has the ability to simulate a general bremsstrahlung spectrum from the basic physical principles. As mentioned earlier, the subroutine that generates the spectrum can handle incident electron beam energies up to the cut-off energy of pair production. A monoenergetic photon beam can be easily simulated too (this is a very trivial problem compared to simulating a bremsstrahlung spectrum. In which case you only specify the energies of all the photons in the incident beam to be a constant).
2. The code interacts with a CAD interface to handle complex geometries.
3. The code can simulate the inspection of assemblies (multiple objects).
4. The code allows the user to change/adjust the angles of the incident and the back scattered radiations and the openings of the collimators.
5. Speed of execution: Each one of the above scans was generated in less than one minute using a DEC5000/240 workstation.

Finally this code is a first step towards developing a more complete description of NDE inspection with back scattering. Several features of the code need to be added to make the results more realistic. These include an open collimation detector simulation. This is a very important feature since an open collimation detector is a common way of using this technique to maximize the resulting signal. A collimated detector makes the experimental setup very tricky and severely reduces the number of photons that hit the detector. The next step in studying and developing this

technique is to compare the results of simulated inspections with experimental results. A trial to get experimental results has shown limited success because of the lack of proper collimation for our IRT320 x-ray generator. Other features that might be added to the code include the simulation of the detector response and the simulation of an array of collimated detectors.

CHAPTER 6. CONCLUSIONS AND FUTURE WORK

This work represents a significant step towards understanding and quantifying the scattering effects of x-rays NDE applications. The buildup factors approach, although an approximate estimate of the scattering effects, fits well within the needs of simulation of x-ray radiography and computed tomography. The most attractive feature about the buildup factors solution was the computational efficiency as compared to Monte Carlo approach or to the solution of the photon transport equation.

As a result of this effort, the following milestones have been accomplished:

1. The concept of buildup factors has been expanded to accommodate a white spectrum of x-rays with energies ranging from few keV's to few hundred keV. This stretching of the definition of buildup factors was supported by intensive experimental and simulation work.
 2. A new Monte Carlo code has been developed: The new code has some unique features like the ability to interact with a CAD interface to handle complex geometries. The code can be executed on either a serial machine or in parallel on a network of UNIX workstations. This last feature reduces the execution time of the code almost linearly with the number of workstations used.
 3. A method to quantify the film undercut effect has been developed. The method
-

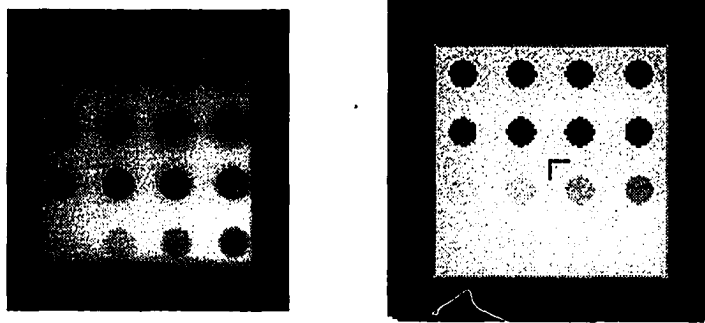


Figure 6.1: A radiographic image of a block of Al with 16 holes of different depths, generated experimentally (left) and generated using XRSIM (right).

needs more accurate information about the film structure and the linear attenuation coefficients of the emulsion layer in the film.

4. A new simulation code for the inspection with Compton back scattering has been developed. The code should guide the users to optimize the inspection parameters.
5. Finally, both the buildup factors results and the undercut simulation have been incorporated into XRSIM to produce a more realistic simulation of the radiography process. The results of integrating both the buildup factors and the undercut simulation into XRSIM are shown in Figures 6.1, 6.2, and 6.3.

Future work will be to generate buildup factors for different materials using different tube energies and different film types. Buildup factors for steel at thickness 0.25 inch were calculated and measured experimentally and the results of the simulation code agreed with the experimental results to within 10%. Also a new CAD interface that has been recently developed can improve the execution time of the

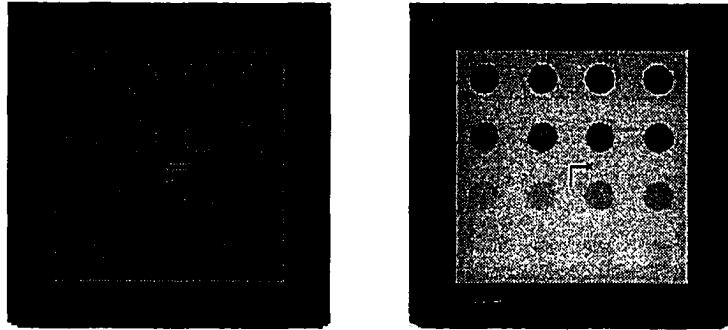


Figure 6.2: Generated using XRSIM with buildup factors (left) and using XRSIM with the film undercut simulation (right).

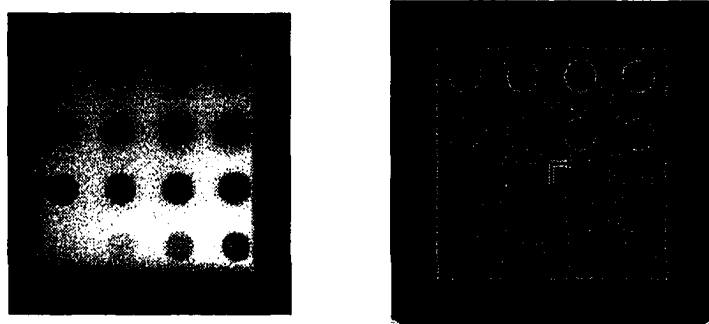


Figure 6.3: Generated experimentally (left) and generated using XRSIM with both the buildup factors and the film undercut simulation integrated into XRSIM.

Monte Carlo code by a factor of 200 [34]. This along with parallel processing of the code will probably give us a speedup of a factor of 2000 as compared to the serial execution of the code.

Studying the film undercut is far from being complete. As the results of this effort have shown, the severity of the undercut phenomenon depends on the film speed. Accurate characterization of the different types of films commonly used in NDE applications is crucial for an accurate simulation of the undercut effect. Integrating this type of unsharpness into XRSIM resulted in a severe increase in the execution time of the code. Careful inspection of the algorithm might result in a significant improvement in the execution time.

Quantitative comparisons of images generated experimentally to those generated by XRSIM showed major discrepancies. This is mainly due to a lack of accuracy in the film model. The model tends to severely overestimate the film density of the simulated images, and hence making the comparison meaningless since buildup factors effect adds to the density of simulated images. A new, more accurate film model is being developed based on the film calibration approach developed in chapter 3. Preliminary results from the new film model along with buildup factors have shown reasonable agreement with experimentally generated images. More specifically, the densities of two different simulated images of two aluminum block with different thicknesses came within 20% of the densities of experimentally generated images. We can not draw decisive conclusion from only two measurements, but certainly the film calibration technique that was developed in chapter 3 is more accurate than the currently used one in XRSIM. Similarly with the film undercut, the lack of accuracy in the current film model prevents us from doing more quantitative comparisons between the results

of the simulation code and the experimental results. The new film model will make this possible in the future.

Compton backscattering is finding more and more usage in NDE. We have developed a code that simulates this inspection technique. The code can be used to optimize the inspection parameters, also to understand and to evaluate the resulting signal. The other half of this work is the experimental confirmation of the results of the simulation code. This will take priority when conducting more work in this area. The code will also be improved to account for open collimation detectors and to use a realistic detector response.

BIBLIOGRAPHY

- [1] Arthur Beiser. "Concepts of Modern Physics". McGraw-Hill Book Company, New York 1981.
 - [2] R. Halmshaw. "Nondestructive Testing". Edward Arnold, London 1987.
 - [3] Lawrence E. Bryant and Paul McIntire. "Nondestructive Testing Handbook". American Society for Nondestructive Testing, Columbus, OH 1985.
 - [4] R. Halmshaw. "The Physics of Industrial Radiology". Heywood Books, London 1966.
 - [5] George L. Becker. "Radiographic NDT". Du Pont NDT Systems, Wilmington 1990.
 - [6] Robert DeNale and Carol Lebowitz. "A Comparison of Ultrasonics and Radiography For Weld Inspection". Review of Progress in Quantitative Nondestructive Evaluation, edited by Donald O. Thompson and Dale E. Chimenti, Vol. 8B, pp. 2003-2010, Plenum Press, New York 1989.
 - [7] Lester W. Schmerr, Jr. and Donald O. Thompson. "NDE and Design - A Unified Life-Cycle Engineering Approach". Review of Progress in Quantitative Nonde-
-

- structive Evaluation, edited by Donald O. Thompson and Dale E. Chimenti, Vol. 12B, pp. 2325-2331, Plenum Press, New York 1993.
- [8] Kenneth S. Krane. "Introductory Nuclear Physics". John Wiley & Sons, New York 1988.
- [9] F. Inanc and J. Gray. "it A CAD Interfaced Simulation Tool For X-ray NDE Studies". Review of Progress in Quantitative Nondestructive Evaluation, edited by Donald O. Thompson and Dale E. Chimenti, Vol. 9A, pp. 391-398. Plenum Press, New York 1990.
- [10] Avinash C. Kak and Malcolm Slaney. "Principles of Computerized Tomographic Imaging". IEEE Press, New York 1988.
- [11] C.M. Lee, L. Kissell, R.H. Pratt, H.K. Tseng. "Phys. Rev.". A13, No.5, pp. 1714-1727, 1976.
- [12] J. Ting, T. Jensen and J.N. Gray. "Using Energy Dispersive X-ray Measurements For Quantitative Determination of Material Loss Due to Corrosion". Review of Progress in Quantitative Nondestructive Evaluation, edited by Donald O. Thompson and Dale E. Chimenti, Vol. 12B, pp. 1963-1969. Plenum Press, New York 1993.
- [13] F. Inanc and J. Gray. "New Development in the Computer Simulation of X-ray Nondestructive Evaluation Process". Review of Progress in Quantitative Non-destructive Evaluation, edited by Donald O. Thompson and Dale E. Chimenti, Vol. 10A, pp. 355-362. Plenum Press, New York 1991.
-

- [14] Carey E. Floyd, Jr., Joseph Y. Lo, Harrell G. Chotas, and Carl E. Ravin. "Quantitative Scatter Measurement in Digital Radiography Using a Photostimulable Phosphor Imaging System". *Med. Phys.* 18(3), pp. 408-413. May/June 1991.
 - [15] Michikata Honda, Katsuya Kikuchi, and Ken-ichi Komatsu. "Method For Estimating The Intensity of Scattered Radiation Using a Scatter Generation Model". *Med. Phys.* 18(2), pp. 219-220. Mar/Apr 1991.
 - [16] Herbert Goldstein. "Attenuation of Gamma Rays and Neutrons in Reactor Shields". Washington, U.S. Govt. Print. Off., 1957.
 - [17] R. Halmshaw. "Industrial Radiology: theory and practice". Applied Science Publishers, London 1982.
 - [18] John R. Lamarsh. "Introduction to Nuclear Engineering". Addison Wesley, Reading, Mass. 1983.
 - [19] Walter R. Nelson, Hideo Hirayama and David W. O. Rogers. "The EGS4 Code System". SLAC-Report-265. December 1985.
 - [20] Jack J. Dongarra, Lain S. Duff, Danny C. Sorensen, and Henk A. Van der Vorst. "Solving Linear Systems on Vector and Shared Memory Computers". Society for Industrial and Applied Mathematics. Philadelphia 1991.
 - [21] "C-Linda User's Guide & Reference Manual v 2.5.2". Scientific Computing Associates Inc. New Haven, Ct. 1993.
 - [22] A. Notea, Y. Bushlin, and U. Feldman. "Secondary Radiation Influence on LSF Shapes in Radiography". *Review of Progress in Quantitative Nondestructive*
-

- Evaluation, edited by Donald O. Thompson and Dale E. Chimenti, Vol. 11B, pp. 363-370. Plenum Press, New York 1992.
- [23] Troy J. Groth. "Computer Modeling of Neutron Radiography". M.S. Thesis, Iowa State University, Ames, Iowa, 1993.
- [24] Valentina I. Wijaya. "Distributed Computing with C-Linda". M.S. Thesis, Iowa State University, Ames, Iowa, 1993.
- [25] A.Fishman, U.Feldman, A.Notea, and Y.Segal. "Point Spread Function Due to Photon Scattering in Iron Radiography". *Material Evaluation*/41/, pp. 1201-1207. September 1983.
- [26] A. A. Harms and D. R. Wyman. "Mathematics and Physics of Neutron Radiography". D. Reidel Publishing company, Hingham, MA, U.S.A. 1986.
- [27] Glenn F.Knoll. "Radiation Detection and Measurement". John Wiley & Sons, New York 1989.
- [28] Arthur B. Chilton, J. Kenneth Shultis and Richard E. Faw. "Principles of Radiation Shielding". Prentice-Hall, Inc., Englewood Cliffs, New Jersey 1984.
- [29] David R. Lide. "Handbook of Chemistry and Physics". Edition 72, CRC Press, Inc. Boston 1992.
- [30] Richard H. Bossi, John L. Cline, Kenneth D. Fridell, and James M. Nelson. "One Sided Radiographic Inspection Using Backscatter Imaging". *Review of Progress in Quantitative Nondestructive Evaluation*. Vol. 8A, pp. 465-471. Plenum Press, New York 1989.
-

- [31] Dale W. Hill and John C. Peak. "Development of a One-Sided Gamma Ray Tomography System". *Review of Progress in Quantitative Nondestructive Evaluation*. Vol. 7A, pp. 415-423. Plenum Press, New York 1987.
- [32] David Hughes. *X-Ray Backscatter Equipment Provides Automatic Screening for Explosives*. *Aviation Week & Space Technology*. April 17, 1989. P. 65-69.
- [33] *Backscatter X-ray Explosives Detector Completes Tests on Heathrow Baggage*. *Aviation Week & Space Technology*. August 10, 1992. P. 35.
- [34] N.Faleel Mohideen. "Unpublished work and personal conversation". Center for Nondestructive Evaluation, Ames, Ia 50011, Jan. 1995.
-